TFAM as a sensor of UVC-induced mitochondrial DNA damage

Dillon E. King[1*], Emily E. Beard[2*], Matthew J. Satusky[3*], Ian Ryde[1], Alex George[1], Caitlin Johnson[2], Emma L. Dolan[4,5], Yuning Zhang[6], Wei Zhu[7], Hunter Wilkins[2], Evan Corden[8], Susan K. Murphy[5], Dorothy Erie[2,9‡], Raluca Gordân[6,7,10‡], and Joel N. Meyer[1‡]
[*]Contributed equally
[‡]Corresponding authors

[1]Nicholas School of the Environment, Duke University
[2]Department of Chemistry, University of North Carolina at Chapel Hill
[3]Renaissance Computing Institute, University of North Carolina at Chapel Hill
[4]Department of Pharmacology, Duke University
[5]Department of Obstetrics and Gynecology, Duke University Medical Center
[6]Department of Biostatistics and Bioinformatics, Duke University
[7]Department of Molecular Genetics and Microbiology, Duke University
[8]Program in Computational Biology and Bioinformatics, Duke University
[9]Lineberger Comprehensive Cancer Center, University of North Carolina at Chapel Hill
[10]Department of Computer Science, Duke University

To whom correspondence should be addressed. Tel: +1 919 613 8109; Email: joel.meyer@duke.edu. Correspondence may also be addressed to Dorothy Erie. Tel: +1 919 962 6370; Email: derie@unc.edu. Correspondence may also be addressed to Raluca Gordân. Tel: + 1 919 684 9881; Email: raluca.gordan@duke.edu

Graphical Abstract:

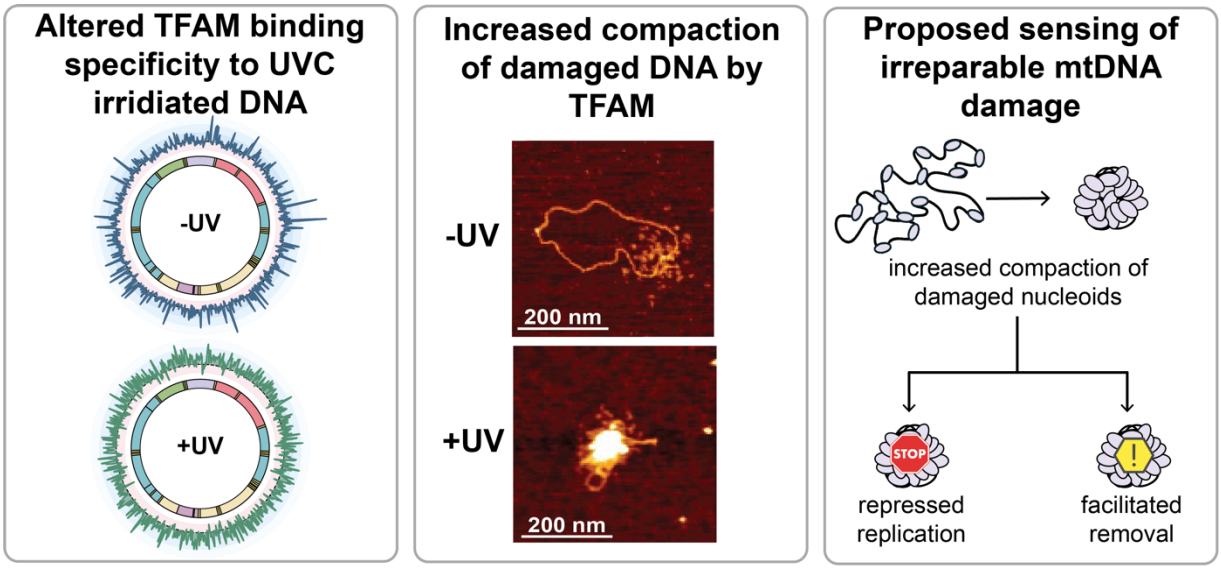

Abstract:
Mitochondria lack nucleotide excision DNA repair; however, mitochondrial DNA (mtDNA) is resistant to mutation accumulation following DNA damage. These observations suggest additional damage sensing or protection mechanisms. Transcription Factor A, Mitochondrial (TFAM) compacts mtDNA into nucleoids. As such, TFAM has emerged as a candidate for protecting DNA or sensing damage. To examine these possibilities, we used live-cell imaging, cell-based assays, atomic force microscopy, and high-throughput protein-DNA binding assays to characterize the binding properties of TFAM to UVC-irradiated DNA and cellular consequences of UVC irradiation. Our data indicate an increase in mtDNA degradation and turnover, without a loss in mitochondrial membrane potential that might trigger mitophagy. We identified a reduction in sequence specificity of TFAM associated with UVC irradiation and a redistribution of TFAM binding throughout the mitochondrial genome. Our AFM data show increased compaction of DNA by TFAM in the presence of damage. Despite the TFAM-mediated compaction of mtDNA, we do not observe any protective effect on DNA damage accumulation in cells or *in vitro*. Taken together, these studies indicate that UVC-induced DNA damage promotes compaction by TFAM, suggesting that TFAM may act as a damage sensor, sequestering damaged genomes to prevent mutagenesis by direct removal or suppression of replication.

Keywords: mitochondria, mtDNA, DNA damage, TFAM, UVC, atomic force microscopy, high-density DNA chips

Introduction:

Mitochondria are complex organelles that play important roles in energy metabolism, cell signaling, regulating immune responses, apoptosis, ion homeostasis, and other functions [1]. Mitochondria contain their own circular double-stranded genome which is approximately 16.5 kilobases in size and encodes 13 proteins, all of which are essential subunits of the electron transport chain (ETC), along with two ribosomal RNAs and 22 transfer RNAs [2]. Mitochondrial DNA (mtDNA) is packaged into 'nucleoid' structures positioned in the inner mitochondrial membrane [3,4]. The mitochondrial nucleoid is composed of over 50 nucleoid-associated proteins involved in maintaining mtDNA and regulating replication and expression [5-8]. The most abundant protein present in the nucleoid is Transcription Factor A, Mitochondrial (TFAM). TFAM alone has been shown to be sufficient *in vitro* to condense and compact mtDNA [9,10]. Within a single mitochondrion, multiple copies of mtDNA exist [11,12] in differing conformations with regard to their nucleoid structure [13]. Notably, the degree of compaction is associated with replication and gene expression activity [14].

mtDNA is more susceptible than nuclear DNA to many damaging agents [15,16], and it lacks some DNA repair pathways that protect the nuclear genome [15-18]. The absence of the nucleotide excision repair (NER) pathway is particularly salient, because it is the predominant DNA repair pathway that can repair damage caused by a wide range of very common environmental pollutants, including polycyclic aromatic hydrocarbons (PAHs), mycotoxins such as aflatoxin B_1, aromatic amines, ultraviolet (UV) light exposure, as well as some drugs such as cisplatin [19]. The process of mitophagy, the selective degradation of mitochondria, contributes to the removal of irreparable mtDNA damage in human cells [20] and *Caenorhabditis elegans* [21-23]. Interestingly, though, despite often incurring high levels of irreparable damage, the mitochondrial genome appears to be highly resistant to mutagenesis from these lesions. Valente *et al.* [24] did not detect mtDNA mutations in somatic cells of mice exposed to the PAH benzo[a]pyrene or the alkylating agent N-ethyl-N-nitrosourea, despite using exposures that caused nuclear DNA mutagenesis and high levels of mtDNA damage. More recently, we reported a similar result in the germline of the nematode *C. elegans* after 50 generations of continuous exposure to the DNA mutagens aflatoxin B_1 or cadmium, even in mitophagy deficient mutants [25]. The lack of mutagenesis in these mitophagy deficient mutants suggest that an unknown cellular mechanism prevents mtDNA mutagenesis.

TFAM is a potential candidate for mutagenesis prevention, because it is known to compact the genome and has been suggested to be a damage sensing protein [26]. TFAM is a multifunctional protein that serves as both a transcription factor [27-29] and a core component of packaging mtDNA [9,10] (Figure S1). TFAM is an unusual transcription factor in that it binds specifically to promoters to initiate transcription but also exhibits high affinity non-specific binding, presumably to facilitate mtDNA packaging. TFAM is a high-mobility group (HMG) protein with two HMG binding domains that bind to DNA [28,30-32]. Once bound to the DNA, TFAM can multimerize, which facilitates looping and ultimately the compaction of the DNA. It has previously been proposed that TFAM may serve as a DNA damage sensing protein for the

mitochondrial genome [26] as TFAM binds differentially to damaged vs. undamaged DNA in the context of oxidative damage [33,34], base loss [35], cisplatin adducts [36], bulged DNA [37], and alkylated lesions [38]. TFAM also interacts with mtDNA repair processes, potentially playing a role in accelerating mtDNA degradation [39] and modulating base excision repair [34]. While most of the forms of mtDNA damage for which TFAM interactions have been characterized can be repaired by mitochondrial base excision repair, interactions between TFAM and irreparable forms of mtDNA damage are less understood.

To further investigate mitochondrial responses to irreparable DNA damage, we characterized cellular responses to ultraviolet-C (UVC) exposure using live-cell imaging and gene expression. We utilized atomic force microscopy (AFM) and protein-DNA binding chips coupled with biochemical assays to characterize TFAM binding to UVC-induced lesions and the structural changes to the compactional status of nucleoids following UVC-induced DNA damage. Additionally, we examined the dependence of UVC DNA damage accumulation and removal on the extent of TFAM-induced compaction of mitochondrial nucleoids. Overall, our data show that cells respond to irreparable mtDNA damage by stimulating mtDNA turnover, in the absence of detectable loss of mitochondrial membrane potential. We also provide evidence that TFAM binding to mtDNA is altered in the context of UVC-induced DNA damage, which may facilitate the recognition of mtDNA damage and the prevention of mutagenesis.

Materials and Methods:

Cell Culture:

HeLa cells were kindly provided by Dr. Chantell Evans (Duke University). TFAM-HA TetOn HeLa S3 cells were kindly provided by Dr. Stefan Isaac and Dr. Stirling Churchman (Harvard University). Cells were grown in DMEM containing glucose and pyruvate (Thermo Fisher Scientific 11995073) supplemented with 10% Fetal Bovine Serum (Thermo Fisher Scientific 10437028), 1% penicillin/streptomycin and maintained at 37°C with 5% CO_2 in a humidified chamber. Cells were routinely tested for mycoplasma contamination and authenticated using STR profiling by the Duke University Cell Culture Facility.

UVC Exposures in Cell Culture:

HeLa cells were grown to 50% confluency. At the time of exposure, media was removed, cells were washed once in PBS, aspirated to remove as much of the PBS as possible to facilitate the effects of the UVC irradiation, and then exposed to UVC using an ultraviolet lamp with built-in UVC sensor (CL-1000 Ultraviolet Crosslinker, UVP, Upland, CA, USA) with peak emission at 254 nm. Following exposure (~1 minute), cell culture media was immediately replaced.

Cell Viability:

To assess cell viability, 10,000 cells were plated in black clear-bottom 96-well plates and allowed to adhere overnight. Cells were washed with PBS and then dosed with UVC as described in the previous sec

tion. Experiments were performed in triplicate with three biological replicates completed for all doses. The 0-, 24-, and 48-hour dose responses were analyzed at their respective time points. Cell viability was assessed using the alamarBlue HS Cell Viability Reagent (Invitrogen) and a FLUOstar Optima microplate reader. The data was analyzed via two-way ANOVA with a Dunnett's correction for multiple comparisons to the control for each time point.

Gene Expression:

Quantitative real-time RT-PCR was performed for *TFAM, POLG, NRF-1, PGC1a, POLRMT*, and *ND-1*. RNA was extracted from HeLa cells using an RNeasy Kit (QIAGEN) and stored at -80°C until analysis. qPCR was performed using the qTower^3 Real-Time PCR System (Analytik-Jena). The *GAPDH* Endogenous Control (Taqman probe ID: Hs02786624_g1, VIC-MGB) and either *TFAM* (Taqman probe ID: Hs00273372_s1, FAM-MGB), *POLG* (Taqman probe ID: Hs00160298_m1, FAM-MGB), *NRF-1* (Taqman probe ID: Hs00602161_m1, FAM-MGB), *PGC1a* (Taqman probe ID: Hs00173304_m1, FAM-MGB), *POLRMT* (Taqman probe ID: Hs04187596_g1, FAM-MGB), or *ND-1* (Taqman probe ID: Hs02596873_s1, FAM-MGB) probes were multiplexed in a 1:1 ratio for each sample. Results for *GAPDH* were used to normalize for RNA input. PCR reactions each contained 100 ng RNA, 0.5µL of each probe, 5µl of Quantabio qScript one-step RT-qPCR ToughMix (QuantaBio) and was brought to a total reaction volume of 10µL with nuclease-free water. Samples were run in triplicate and PCR cycling conditions were as follows: 50°C for 10 minutes, followed by 95°C for one minute, followed by 40 cycles of 95°C for 10 seconds and 60°C for one minute. To examine expression of each gene, the delta delta CT method was used to calculate fold change in gene expression. The data were analyzed via two-way ANOVA with Dunnett's post-hoc test for multiple comparisons.

Mitochondrial Membrane Potential:

HeLa cells were plated and allowed to attach and proliferate for 24 hours. Then, cells were exposed to either 0, 10, 30, or 50 J/m^2 of UVC. Cells were harvested and stained to acquire by flow cytometry at 6 and 24 hours post UVC exposure. Each UVC dose had a tetramethylrhodamine, methyl ester (TMRM)-stained sample and an unstained control. Non-UVC-exposed cells from each timepoint had additional TMRM-stained tubes for carbonyl cyanide-p-trifluoromethoxyphenylhydrazone (FCCP) positive controls. Cells were aliquoted (4.0 X 10^5 per sample) and washed with PBS. Samples were stained in 1 mL of Live Cell Imaging Medium with a final concentration of 15 nM TMRM for 20 minutes. TMRM was left in cell suspension during flow acquisition. Samples were acquired on a BD FACSCanto-II flow cytometer using the blue laser (488 nm) and the 585/42 detection filter to excite and detect TMRM. Events were gated to include live, single cells, and 10,000 events were acquired from

this population. Immediately before their acquisition, TMRM-stained control cells were spiked with 5 μM FCCP. The FCCP positive control was incubated for 5 min before acquiring. In FlowJo, live cells were manually gated in a FSC-A vs SSC-A plot, then single cells were gated in a FSC-A vs FSC-H plot. Median fluorescence intensity (MFI) was tabulated for the histogram of each sample. Background fluorescence from the unstained sample of each UVC dose was subtracted from the corresponding stained samples. The average and standard error of three experiments were plotted. Data was analyzed via two-way ANOVA for treatment and timepoint.

Live Cell Imaging:

HeLa cells (1.5 X 10^3) were seeded onto 35 mm glass bottom well petri dishes (Mattek) and allowed to adhere. After 48 hours in culture, cells were washed once with PBS and then exposed to either 0 or 10 J/m^2 UVC as described previously. Cells were then immediately incubated with picogreen at a concentration of 1 μL/mL of medium for 1.5 hours to stain mtDNA. Cells were then washed three times and given fresh media. Twenty-four hours after the UVC exposure, cells were incubated with lysotracker red (75 nM), mitotracker deep red (150 nM), and 7 μg/mL Hoescht 33342 for 30 minutes, again followed by three quick washes, and then placed in imaging medium. Cells were imaged in an environmental chamber at 37°C in an Andor Dragonfly 505 unit with Borealis illumination spinning disk confocal 100x/1.40-0.70 HCX PL APO (Leica 11506210) oil-immersion objective and an Andor iXon Life 888 1024x1024 EMCCD camera.

Confocal Image Analysis:

Images were deconvoluted using Huygens SVI deconvolution software. For each channel, images were segmented in Labkit [40]. Segmented images were used to quantify area of the cell, area of mitochondria, mitochondrial morphology parameters, number of picogreen spots, and number of lysosome spots. To assess lysosome colocalization, object-oriented colocalization [41] was performed on segmented images using a custom Python script. At least 30 cells in each treatment group were analyzed from three independent biologic replicates. The data were analyzed via two-tailed unpaired t-test.

Quantification of DNA Damage:

To determine the lesion frequency associated with mitochondrial DNA, a quantitative long-range PCR assay was used [42]. For cell samples, DNA was isolated from frozen cell pellets using genomic tips (Qiagen). QPCR was run on the samples to generate a long product (~10kb) as well as a short product (~200 bp). Given the ability for DNA damage to block the DNA polymerase used in this PCR, the amount of damage is then calculated based on the amount of amplification. The long product is used to calculate reduced amplification compared to the controls, whereas the short product is used to normalize sample to sample variability in mitochondrial DNA copy number. The data were analyzed via two-way ANOVA with a Dunnett's post-hoc test for multiple comparisons.

TFAM Overexpression:

TFAM-HA TetOn HeLa S3 cells were grown in six-well dishes to a confluency of 50% and treated with 100 ng/mL doxycycline for 48 hours. Cells were provided fresh media every 24 hours for the duration of the experiment. UVC exposure was performed as described above with cells exposed to either 0, 10, 30, 50, 70, or 100 J/m^2. mtDNA damage was quantified at 0 hours, 24 hours, and 48 hours following UVC exposure as described previously and cell viability was assessed. TFAM overexpression levels in control samples were confirmed by real-time PCR and western blot analysis. Real-time PCR to assess *TFAM* gene expression was performed as described above.

For western blot analysis, cells were washed twice in ice-cold PBS, and then lysed using RIPA buffer containing a protease inhibitor cocktail. Protein content was determined using a BCA Assay (Pierce). Protein lysate (30 µg/well) was loaded into a 10% SDS-PAGE gel. Gels were transferred onto activated PVDF membrane, followed by immunoblot. Densitometry was performed using ImageJ. TFAM was normalized to β-actin and samples were compared between doxycycline treatment groups at their respective time points. Antibodies used were anti-TFAM antibody (Santa Cruz sc-376672) and an anti-β-Actin antibody (Sigma A5441). The data were analyzed via two-way ANOVA.

Purification of Human TFAM:

Human_TFAM_NoMTS_pET28 was a gift from David Chan (Addgene plasmid # 34705; http://n2t.net/addgene:34705 ; RRID:Addgene_34705). Recombinant human TFAM was purified as previously described [30], flash frozen in liquid nitrogen and stored at -80°C. Protein concentration was determined using a Qubit Protein BR Assay (Thermo A50668).

Generation of Substrates for Atomic Force Microscopy:

To assess alterations in TFAM compaction of DNA in the context of UVC-induced lesions, we assessed TFAM binding to circular pUC19. Levels of UVC exposure were chosen based on previous dose response curves performed on naked mtDNA indicating a linear increase in lesions associated with increasing UVC exposure, where 10 J/m^2 results in roughly 1 lesion per 10kb [43]. Given the similar content of adjacent pyrimidine bases (whole mitochondrial genome: 535/kb; 8.9kb product used in mtDNA damage assay: 532/kb; and pUC19: 510/kb), we exposed the pUC19 (2.686 kb in size) to 100 J/m^2 to induce roughly three lesions per DNA molecule.

Atomic Force Microscopy:

Undamaged or damaged DNA (1.5 ng/µL) was incubated for two minutes on ice with varying concentrations of TFAM in 25 mM HEPES, 10 mM $Mg(OAc)_2$, 25 mM NaOAc, 75 mM K(OAc), pH 7.5, then deposited onto ethanolamine treated mica and imaged in air using a JPK NanoWizard 4 XP in tapping mode. Mica was treated with ethanolamine by vapor deposition in

a desiccator by aliquoting 20 µL of ethanolamine stock onto a piece of parafilm and placing it into the desiccator with freshly peeled mica for 15 minutes to allow time for the ethanolamine to vaporize and transfer onto the mica surface. Cantilevers used were PPP-NCHR (Nanoworld, Matterhorn, Switzerland) with nominal resonance frequencies of 330 kHz. Images were taken at a 2.0 x 2.0 µm area for small DNA fragments such as pUC19 while the full-length mitochondrial DNA images were between 2-5 µm. Images of TFAM and small DNA oligonucleotides were taken at a 1.0 x 1.0 µm area on untreated mica. All AFM images were taken with a resolution of 512 x 512 pixels, and a scan rate of 2 Hz. Additionally, each TFAM-DNA complex with pUC19 was categorized into three different categories: dispersed, intermediate, or punctate, based on the degree of observable DNA compaction and height of the TFAM nucleoid structure.

Images were analyzed using the MATLAB program ImageMetrics (https://imagemetrics.wordpress.com/) in MATLAB version R2020b (MathWorks, Natick MA) . Images were line-wise flattened, and subsequently, a threshold was applied to isolate the individual protein only or protein-DNA complexes on the surface. For each of these complexes or proteins, the volume, area, and height were recorded. Histograms of the volumes of TFAM protein alone or in the presence of DNA were generated from the data using MATLAB version R2020b.

We used AFM to determine the oligomerization state of TFAM bound to some DNA oligonucleotides (33 base pairs) used for the fluorescence anisotropy studies. TFAM (30 nM) was incubated on ice in the absence or presence of DNA (10 nM) for two minutes, deposited on the surface, rinsed, and dried with N_2. ImageMetrics was used to determine the volumes of the individual particles on the surface as described earlier. The AFM volume of proteins are directly proportional the protein molecular weight allowing determination of the oligomerization state [44-47]. The oligomerization states are determined from histogram plots of the distribution of volumes that were generated in MATLAB version R2020b.

In vitro Nucleoid Reconstitution:

Full-length linear mtDNA was generated by long-range PCR amplification using the following primers; F, 5‘ – GGT TCA GCT GTC TCT TAC TTT TAA CCA GTG – 3’ and R, 5‘ – CTC GTG GAG CCA TTC ATA CAG GTC – 3’. Genomic DNA was isolated from HeLa cells using the Qiagen QiAmp DNA Mini Kit according to the manufacturer’s instructions and used as template DNA. PCR reactions were carried out using 100 ng template in 50 µL reactions with LongAmp Hot Start Taq Polymerase (New England Biosciences). DNA was amplified using a two-step amplification protocol: 95°C for 2 minutes, 30 cycles of 95°C for 20 seconds and 68°C for 13 minutes, and a final extension at 68°C for 18 minutes. PCR product was then purified using a Zymo Genomic DNA Clean & Concentrator kit (Zymo Research D4011) and the DNA concentration was determined using a Nanodrop One (Thermo Scientific).
In vitro nucleoids were generated in 50 µL reactions, containing 20 ng/µL full-length linear mtDNA with 0, 100, 250, or 1000 nM TFAM (added last) in binding buffer (25 mM HEPES pH 7.5, 75 mM KOAc, 25 mM NaOAc, 10 mM $Mg(OAc)_2$). The degree of compaction of the

mtDNA at these TFAM concentrations was confirmed using AFM as described earlier. After the addition of TFAM, reactions were incubated on ice for two minutes, then deposited as a 50 μL drop onto a petri dish lid and then immediately exposed to either 0, 5, 10, 30, or 50 J/m^2 UVC. Following UVC treatment, a Zymo Genomic DNA Clean & Concentrator 10 kit (Zymo Research D4011) was used to remove the protein, and the DNA concentration was determined using a Nanodrop One (Thermo Scientific). Samples were diluted to 25 pg/μL and levels of mtDNA damage were quantified as described above.

High-throughput, High-resolution Binding of TFAM to the Mitochondrial Genome:

High-density DNA chips (or arrays) printed with oligos covering the entire mitochondrial genome at a 2-bp resolution were used to measure TFAM binding in the presence and absence of UV-induced damage. Single-stranded DNA arrays were purchased from Agilent in a 4 × 180 k format containing four identical chambers with 176,024 DNA spots in each chamber. The DNA library synthesized on the array contained the entire mitochondrial genome in 33-nt variable sequences and a 27-nt primer binding sequence. A sliding window approach was used to partition the hg38 human mitochondrial genome into overlapping 33-nt regions, where each sequential window was shifted by 2 nt along the mtDNA sequence (the single 'N' was replaced with a cytosine). For every mtDNA window, an additional DNA sequence was generated using the reverse compliment of the window, such that the full genome was synthesized de novo in both the 5' to 3' and 3' to 5' orientations on the glass slide. TFAM binding to a universal DNA library containing all possible 7-mers [48] was performed prior to library designs to determine the range of binding specificity, optimize the final protein concentration to be used, and select low affinity non-mitochondrial probes to include in the sequence library for normalization purposes. The number of replicate spots for each sequence on the array was 10. In total, there were 8,285 unique probes on the array corresponding to the mitochondrial genome.

The DNA was double stranded on the arrays via primer extension, as described previously [48], and then subjected to UVC irradiation to damage DNA in two of the chambers on the array, as previously described [49]. Finally, purified TFAM as well as Penta-His Alexa 488 (Qiagen) were incubated in the chambers in TFAM binding buffer (25 mM HEPES, 10 mM $Mg(OAc)_2$, 100 mM NaOAc, pH 7.5) as previously described [50] and the fluorescent signal associated with bound protein for each DNA spot was determined using a GenePix® 4400A microarray scanner and the GenePix® Pro 7.3 software. The assay was performed using a final concentration of either 30 nM or 300 nM TFAM. In total, assays were run at 30 nM TFAM with and without UVC as well as 300 nM TFAM with and without UVC.

Fluorescence intensity values for each spot were normalized via detrending, as previously described [50]. Mean, median, standard deviation, and standard error were calculated from normalized fluorescence intensity values across the 10 replicates for each spot. Kernel density estimates were calculated for the fluorescence values of the bottom universal binders for the conditions in each chamber, and a Gaussian curve was fit to those data. For each chamber, the mean and standard deviation estimates from the Gaussian fit were used to convert all median

fluorescence intensity values into TFAM binding z-scores, which reflect the DNA binding specificity of TFAM under that experimental condition. Given that the assay was performed on sequences generated in 5' to 3' orientation as well as a 3' to 5' orientation, the maximum z-score obtained from each orientation (*i.e.*, whichever was higher) was used to generate binding plots. Plots were then smoothed using a 22-nt window, in order to account for the 22-nt footprint of TFAM binding. Most binding z-scores are expected to be low, regardless of the binding conditions, as most sequences are expected to show some low background level of binding. However, under conditions where TFAM binds DNA with high specificity, we expect the array-based assay to also identify sequences with high z-score, *i.e.*, sequences that TFAM can bind with higher occupancy, and distinguish them from background. In contrast, conditions where all z-scores are generally low are indicative of low binding specificity throughout, as all sequences are bound similarly by TFAM, and no particular target sites stand out. All statistics were performed using a custom Python notebook.

Fluorescence Polarization:

Sequences representing a broad range of z-scores from the array-based experiments (Table 1) were ordered from Integrated DNA Technologies as HPLC-purified, double-stranded oligos (reverse complement not shown in table) with a 5' 6-carboxyfluorescein modification on the strand listed. Each sequence was tested with and without 1,500 J/m^2 UVC irradiation to match conditions used in the array-based assay. Each condition was tested in triplicate.

TFAM was serially diluted in binding buffer (25 mM HEPES, 10 mM $Mg(OAc)_2$, 25 mM NaOAc, 75 mM K(OAc), pH 7.5) from 15 to 0 nM on ice. Dilutions were then mixed in a low-binding Costar 96-well half-area black well plate (Corning, Corning, NY) with DNA diluted in binding buffer, for a final DNA concentration of 1 nM and volume of 55 µL in each well. Plates were read with a PHERAstar microplate reader from BMG Labtech (Cary, NC) using an FP filter with excitation at 485 nm and emission at 590 nm. Anisotropy was calculated with Equation 1:

$$r = \frac{I_{\parallel} - I_{\perp}}{I_{\parallel} + 2I_{\perp}} \qquad \textbf{Eq. 1}$$

where r is anisotropy and $I_{\parallel}$ and $I_{\perp}$ are fluorescence intensity in the parallel and perpendicular direction, respectively. Anisotropy was then plotted against TFAM concentration and fit to Equation 2:

$$r = r_f + \frac{r_b \cdot [TFAM]^n}{K_D{}^n + [TFAM]^n} \qquad \textbf{Eq. 2}$$

where r_f is the fraction of signal from free DNA, r_b is the fraction of signal from bound DNA, [TFAM] is TFAM concentration, n is the Hill coefficient, and K_D is the dissociation constant. The variance σ^2 associated with the each of the derived K_D and n values from individual fits was

identified from the diagonal of the covariance matrix, and the inverse-variance weighted mean $\bar{x}_{wtd}$ and standard error $(\sigma_{\bar{x}})_{wtd}$ were calculated using Equations 3 and 4, respectively, across the three experimental replicates:

$$\bar{x}_{wtd} = \frac{\sum_{i=1}^{m} x_i/\sigma_i^2}{\sum_{i=1}^{m} 1/\sigma_i^2} \qquad \textbf{Eq. 3}$$

$$(\sigma_{\bar{x}})_{wtd} = \sqrt{\frac{\left(\frac{\sum_{i=1}^{m} {x_i}^2/\sigma_i^2}{\sum_{i=1}^{m} 1/\sigma_i^2} - {\bar{x}_{wtd}}^2\right)\left(\frac{m}{m-1}\right)}{m}} \qquad \textbf{Eq. 4}$$

where x_i is the derived value from each fit, m is the number of replicates in the condition [51]. Curve fitting and statistical analysis were performed in Python.

Table 1: Sequences used for TFAM K_D measurements:

Oligonucleotide name	**Sequence (5' – 3')**
ND1_288	CTC CAC ACT AGC AGA GAC CAA CCG AAC CCC CTT
COX2_229	GCC CCC ATT CGT ATA ATA ATT ACA TCA CAA GAC
TRNT_10	CTT GTA GTA TAA ACT AAT ACA CCA GTC TTG TAA
ND2_401	CAA ATG GGC CAT TAT CGA AGA ATT CAC AAA AAA
ND3_92	TTA GTA GCT ATT ACC TTC TTA TTA TTT GAT CTA
ND1_450	ACT CAC CCT AGC ATT ACT TAT ATG ATA TGT CTC
ND6_87	TTC CTA CAC TAT TAA AGT TTA CCA CAA CCA CCA
RNR2_619	ATT GAT CCA ATA ACT TGA CCA ACG GAA CAA GTT
COX1_27	AAG ACA TTG GAA CAC TAT ACC TAT TAT TCG GCG
ND4_473	CGG CGC AGT CAT TCT CAT AAT CGC CCA CGG GCT
ND1_353 40mer	CAC AAA CAT TAT TAT AAT AAA CAC CCT CAC CAC TAC AAT C
ND1_353	ATT ATT ATA ATA AAC ACC CTC ACC ACT ACA ATC

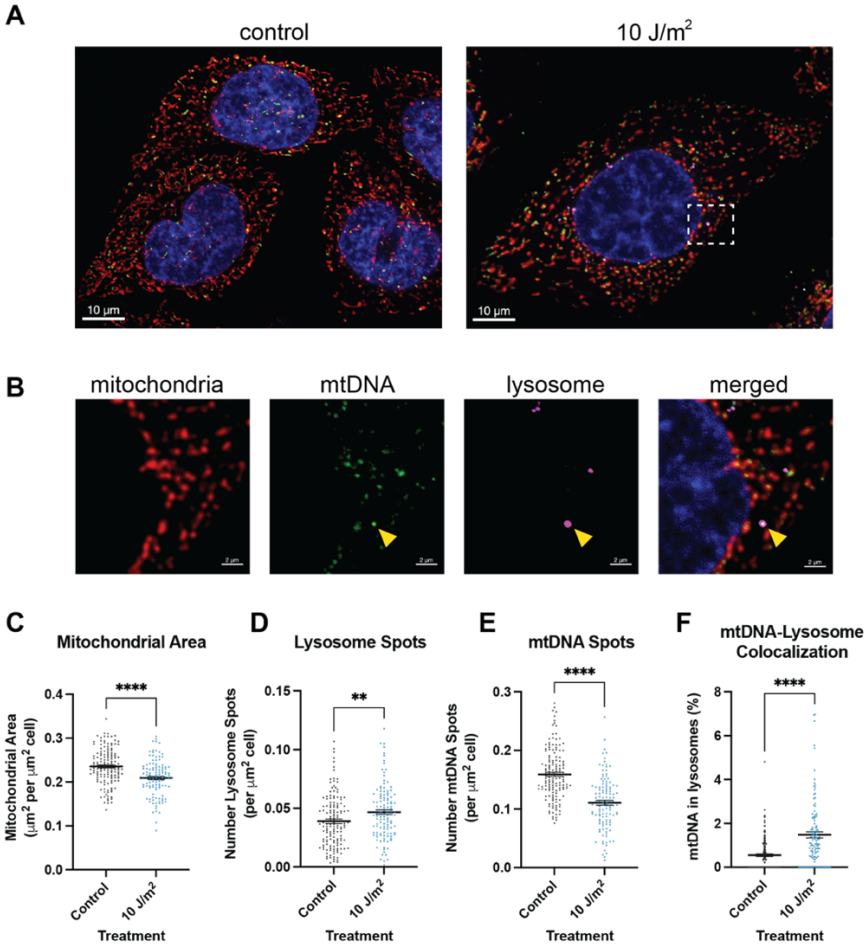

Figure 1: Live-cell imaging following UVC treatment indicates increased mtDNA degradation.

A) Representative images for control (left) and UVC treated (right) cells. Merged channels include mitotracker (red, stains mitochondria), lysotracker (pink, stains lysosomes), picogreen (green, stains mtDNA), and nuclei (blue). **B)** Inset outlined in the UVC treated cells in panel A. Channels from left to right include mitochondria, mtDNA, lysosome, and the merged image. The yellow arrow indicates a mtDNA spot colocalized with lysotracker. For panels C-F, x-axes represent the treatment and data was analyzed via two-tailed unpaired t-test. Data includes at least n=30 cells per treatment group per imaging session and three distinct imaging sessions. **C)** Quantification of the total mitochondrial area per cell normalized to the size of the cell ($p<0.0001$). **D)** Quantification of the number of lysosomes normalized to the size of the cell ($p=0.0054$). **E)** Quantification of the number of mtDNA spots normalized to the size of the cell ($p<0.0001$). **F)** Quantification of the proportion of mtDNA spots within lysosomes ($p<0.0001$).

Results:

Cells increase mtDNA turnover following mtDNA damage from UVC exposure:

We used multicolor live-cell imaging to investigate alterations to mitochondrial morphology and possible lysosomal degradation of mtDNA following UVC exposures, following confirmation that low doses of UVC are not associated with decreases in cell viability (Figure S2). We performed live-cell imaging on HeLa cells exposed to either 0 or 10 J/m^2 UVC following a 24-hour recovery time after the exposure, staining for mtDNA, lysosomes, mitochondria, and nuclei (Figure 1A, 1B) and quantifying number of mtDNA spots, lysosome spots, area of mitochondria, and colocalization of lysosomes and mtDNA. Because we observe larger cell areas in the UVC treated group (Figure S3A), we normalized our data to the area of each cell. Our data indicate a decrease in the total area of mitochondria in UVC treated cells (Figure 1C), but no significant differences in the mitochondrial morphology present in either treatment group, measured by the mean area of individual mitochondria or the mean perimeter (Figure S3B, Figure S3C), although there is a modest decrease in mean eccentricity (Figure S3D). Notably, however, the cells exhibit an increase in the total number of lysosomes per cell (Figure 1D) and a decrease in the number of mtDNA spots (Figure 1E). Furthermore, a higher proportion of mtDNA colocalizes with lysosomes in the UVC treated cells versus the controls (Figure 1F, representative image in Figure 1B). Taken together, these results suggest increased mtDNA degradation.

To confirm the increase in mtDNA degradation, we assessed levels of mtDNA damage and mtDNA copy number immediately following exposure to UVC and after 24 and 48 hours of recovery time. Immediately after damage, we observe a dose-dependent increase in mtDNA lesions with UVC exposure (Figure 2A). After 24 hours, we observe a decrease in mtDNA damage levels, with significant levels of damage still present in cells exposed to 30 J/m^2 (Figure 2A). After 48 hours, damage is below the limit of detection (Figure 2A). Alongside the decreased mtDNA damage at 24 hours following exposure, there is a modest decline in the ratio of mtDNA to nuclear DNA (Figure 2B), indicating removal of mtDNA. This result rules out the possibility that the decreased average level of mtDNA damage we observed at 24 hours resulted from dilution of damage. Both the decline in mtDNA copy number (Figure 2B) and our live-cell imaging observations of reduced mtDNA spots and increase in colocalization with lysosomes (Figure 1E-F) are consistent with increased degradation. After 48 hours of recovery time, the ratio of mtDNA to nuclear DNA is increased (Figure 2B), indicating that the cells have replenished their mtDNA levels. Taken together, these results indicate that mtDNA turnover (removal and replacement) occurs after UVC-induced damage.

Given that replication of mtDNA is required to replenish copies of the mitochondrial genome during turnover, we assessed mRNA levels of key genes (*TFAM*, *PGC1α*, *NRF-1*, *POLRMT*, *POLG*, *ND-1*) associated with mtDNA replication and transcription following exposure to UVC. TFAM is responsible for initiating transcription, and it also plays a role in replication, because mtDNA transcription is coupled to mtDNA replication. TFAM expression is regulated by NRF-1, which is regulated by PGC1α. POLRMT is the mitochondrial RNA

polymerase, which is necessary for transcription as well as replication as it generates primers to initiate mtDNA replication. POLG is the catalytic subunit of the DNA polymerase responsible for DNA synthesis during mtDNA replication. *ND-1* is a transcript of the mitochondrial genome that we utilized to assess mtDNA transcriptional activity.

We observe downregulation of *PGC1α* and *NRF-1* transcripts starting at 4 hours after exposure to UVC until 24 hours (Figure S4A, Figure S4B), at which point, *PGC1α* transcripts increase (Figure S4A), followed by elevation of *NRF-1* transcripts at 48 hours (Figure S4B). Interestingly, downregulation of *PGC1α* and *NRF-1* at the earlier time points is not associated with downregulation of *TFAM* (Figure 2C). Following a 24-hour recovery after exposure, we observe upregulation of *TFAM* (Figure 2C), *POLG* (Figure 2D), and *POLRMT* (Figure 2E), but not *ND-1* (Figure 2F). These results indicate that mtDNA replication occurs alongside the decrease in copy number observed 24 hours after exposure (Figure 2B). After a 48-hour recovery period, mtDNA copy number is replenished (and in fact increased, at the lower UVC exposure; Figure 2B), and *TFAM* (Figure 2C), *POLRMT* (Figure 2E) and *ND-1* are upregulated (Figure 2F), suggestive of increased transcriptional activity.

A loss of mitochondrial membrane potential is an indirect mechanism that often allows for detection of mitochondrial dysfunction and induction of mitophagy; however, we did not detect a loss of membrane potential in cells exposed to UVC (Figure 2G). Notably, these results suggest that the mtDNA turnover following damage does not result from indirect sensing of generalized mitochondrial dysfunction and further suggests that there may be a direct damage sensing mechanism.

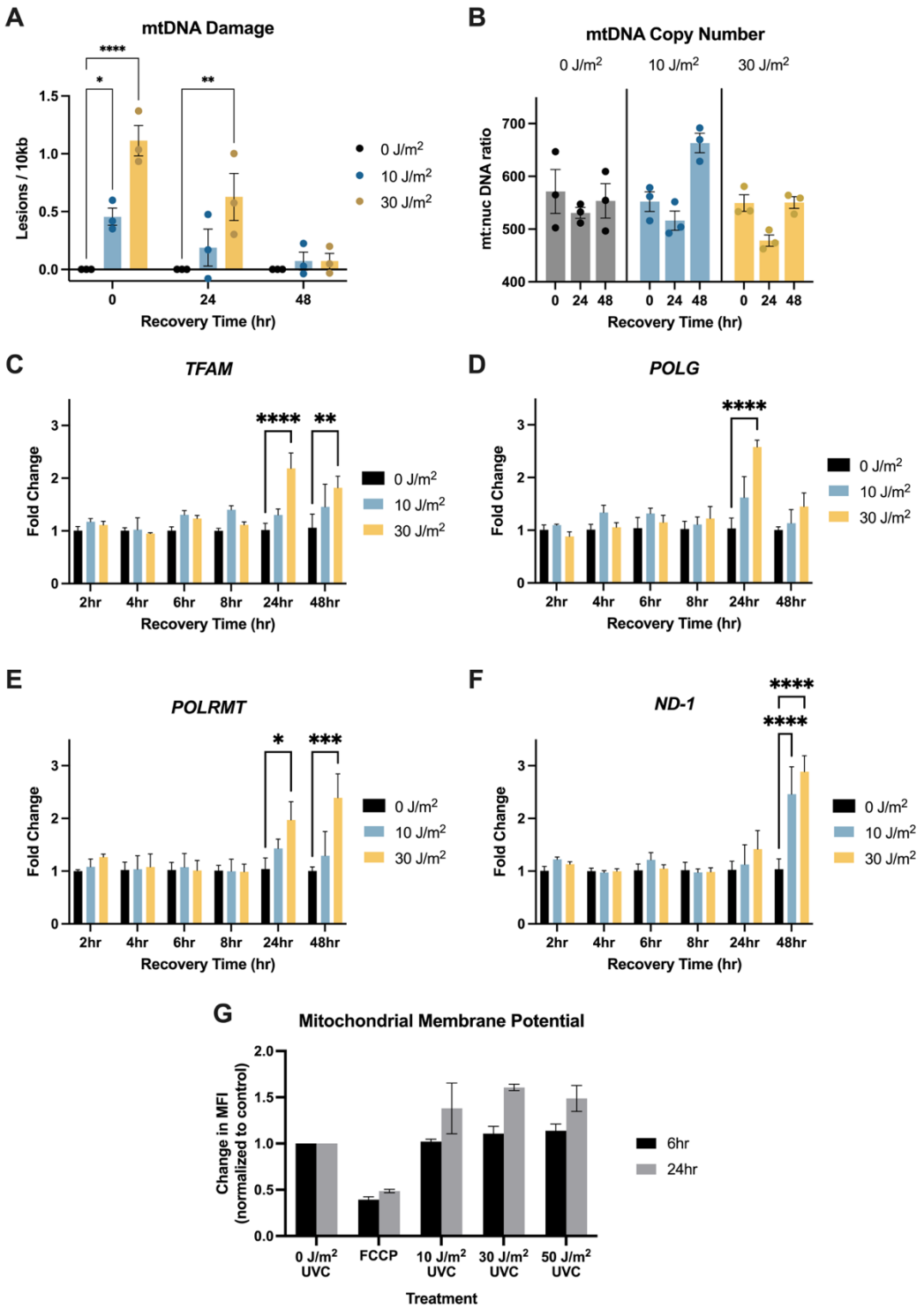

Figure 2: UVC exposures stimulate mtDNA turnover to remove mtDNA damage, upregulation in mtDNA replication genes, and increase mitochondrial transcription in the absence of apparent mitochondrial dysfunction.

For panels A-F, x-axes represent recovery time, i.e., time following the UVC exposure. Doses of UVC used were 0, 10, and 30 J/m^2. **A)** Mitochondrial DNA damage levels following UVC

exposure. Y-axis represents the level of damage (lesions/10kb). Data analyzed via two-way ANOVA with a Dunnett's post-hoc test for multiple comparisons (dose: $p<0.0001$, time: $p=0.0001$, interaction: $p=0.0024$). **B)** Ratio of mitochondrial to nuclear copy number after exposure to UVC at 0, 24, and 48 hr post exposure. Y-axis represents the ratio of mtDNA copy number to nuclear DNA copy number. Data analyzed via two-way ANOVA (dose: $p=0.015$, time: $p=0.008$, interaction: $p=0.11$). For panels C-F, y-axes represent fold change normalized to the control (0 J/m^2) at each timepoint. All data was analyzed via two-way ANOVA with Dunnett's post-hoc test for multiple comparisons. **C)** *TFAM* expression level assessed via qPCR following UVC exposure (dose: $p=0.004$, time: $p=0.001$, interaction: $p=0.02$). **D)** *POLG* expression level assessed via qPCR following UVC exposure (dose: $p=0.002$, time: $p=0.003$, interaction: $p=0.004$). **E)** *POLRMT* expression level assessed via qPCR following UVC exposure (Dose: $p=0.015$, time: $p=0.009$, interaction: $p=0.12$). **F)** *ND-1* expression level assessed via qPCR following UVC exposure (Dose: $p<0.0001$, time: $p=0.006$, interaction: $p=0.003$). **G)** Mitochondrial membrane potential assessed via flow cytometry following exposure to 0, 10, 30, or 50 J/m^2 UVC at 6 and 24 hours after exposure. The x-axis represents the exposure group and the y-axis represents the change in Median Fluorescent Intensities (MFI) of TMRM normalized to the control for each timepoint. Cells were also exposed to FCCP, a well-known chemical that causes mitochondrial depolarization, as a positive control. Data was analyzed via a two-way ANOVA (treatment: $p=0.0008$, time: $p<0.0001$, interaction: $p=0.14$).

High-throughput in vitro data reveals that UVC-induced damage alters TFAM binding specificity across the mitochondrial genome:

The preceding results suggest that cells might directly sense mtDNA damage. The observations that TFAM can compact DNA *in vitro* [9,10] and exhibits differential binding to damaged DNA [26] suggest that it could potentially serve as a damage sensor. In addition, TFAM plays a role in maintaining mtDNA copy number and regulating both transcription and replication [27-29,52]. These functions may allow TFAM to either "tag" genomes for degradation or sequester them from transcription and replication proteins.

In general, the specificity of TFAM binding across the mitochondrial genome is not well understood. There are conflicting reports on the specificity with which TFAM binds different regions of the mitochondrial genome, with some indicating specificity for promoter regions [53,54], and others reporting relatively uniform binding across the genome [55,56]. To address these gaps in knowledge and be able to compare TFAM binding to damaged vs. undamaged mtDNA, we leveraged an *in vitro* DNA-chip based technology [48] to measure TFAM binding to tens of thousands of short DNA sites simultaneously.

We designed a custom library to cover the entirety of the human mitochondrial genome using a sliding 33-nucleotide window width with a 2-nucleotide shift for each consecutive probe (Figure S5). A subset of the chambers was irradiated with UVC to induce photolesions on the DNAs. We then incubated the chambers with either 30 nM or 300 nM TFAM (Figure S5). The concentrations of TFAM were selected based on preliminary experiments to ensure fluorescence

intensity values were well within the range of detection. We were able to identify locations in the mitochondrial genome at which TFAM exhibits high occupancy and observed changes in sequence specificity of TFAM binding in the context of UVC-irritated DNA.

To assess sequence specificity, we normalized TFAM binding levels by converting the fluorescence intensity values to z-scores using a control distribution based on 116 non-mitochondrial low affinity sequences previously identified in a TFAM universal protein-DNA binding array experiment (Methods, Figure S6). Our data reveal high-occupancy TFAM binding sites within the mitochondrial genome that are preferentially bound at the low concentration (30 nM) of TFAM, as indicated by the peaks in the z-scores plotted across the mitochondrial genome (Figure 3). At the high TFAM concentration (300 nM), peaks in binding occupancy occur at the same locations in the genome; however, their z-scores are lower due to the overall increase in TFAM binding to all sequences (Figures S7 and S8). We observe a strong correlation in z-scores between probes in the 30 nM and 300 nM datasets, further supporting the specificity of TFAM binding even at a high TFAM concentration (Figure S8). Previously, it has been suggested that the minimal binding motif for TFAM is two guanines, separated by 10 random nucleotides, referred to as a $GN_{10}G$ motif [32] because all four TFAM promoter sequences contain this motif and crystal structures indicate interactions between TFAM and the guanine nucleotides in this motif [32,57]. Our data, however, does not support this hypothesis. Specifically, the distributions of z-scores for sequences with and without the $GN_{10}G$ motif are striking similar (Figure S9). Comparison of our data with previously published *in vivo* mitochondrial DNase I footprints [53] show strong overlap between the two data sets (Figure S10), suggesting that these data may be representative of *in vivo* TFAM binding.

mtDNA contains four promoters that are regulated by TFAM: two on the heavy strand (HSP1 and HSP2) and two on the light strand (LSP1 and LSP2). Within promoter regions of the mitochondrial genome, we observe peaks in z-scores at both LSP1 and HSP1, but not LSP2 and HSP2 promoters (Figure 3, Figure S11). Interestingly, the z-scores at these sites appear to be lower than many of the high-occupancy sites identified throughout the genome (Figure 3A). Although perhaps surprising at first glance, previous work also indicates a lack of enrichment of TFAM at promoter sequences *in vivo* [55], and modest footprints of TFAM binding at promoter sites *in vitro* [57].

In contrast to the distinct peaks in the z-scores that we observe with non-irradiated DNA, experiments performed on irradiated DNA show more uniform binding patterns and lack of distinct peaks in the z-scores throughout the mitochondrial genome (Figure 3B). These results suggest that the UVC damage reduces sequence specificity of TFAM. To examine this finding more systematically, we plotted the distribution of z-scores associated with the probes that are in the top 5% of z-scores and the bottom 5% of z-scores in the context of non-damaged DNA and UVC-irradiated DNA (Figure S12A-B). The z-scores of our top binders (*i.e.*, probes for which TFAM exhibits high specificity) decrease after UVC irradiation (Figure S12A), whereas the z-scores of our weakest binding sequences (*i.e.*, probes for which TFAM exhibits little to no preference) increase after UVC irradiation (Figure S12B). In addition, plotting the median z-

score in the non-UVC-irradiated chamber against the change in z-score after UVC-irradiation reveals a strong negative correlation, further supporting a reduction in sequence specificity upon UVC irradiation (Figure S12C).

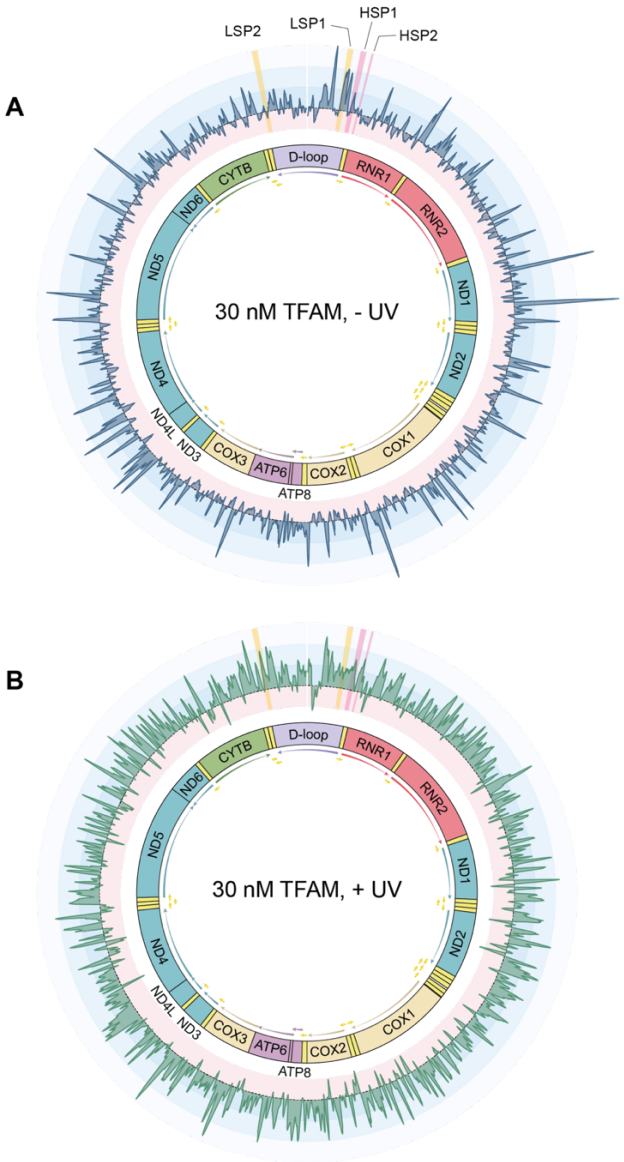

Figure 3: TFAM has specific binding across the mitochondrial genome and exhibits a reduction in specificity in the context of UVC-irradiated DNA.
The median z-score plotted to the coordinate of the middle nucleotide of the variable mitochondrial region of the sequence for the non-UVC-irradiated chamber containing 30 nM TFAM (**A**) and the UVC-irradiated chamber containing 30 nM TFAM (**B**). The gene map of the mitochondrial genome is shown in the center. Z-score variation is color coded such that positive

z-scores associated with high binding are in in blue, and progressively get lighter as the z-scores get higher. Negative z-scores associated with low binding are in red. Regions highlighted in yellow are the promoter sequences of the mitochondrial genome on the light strand (LSP1 and LSP2), while regions highlighted in pink are the promoter sequences on the heavy strand (HSP1 and HSP2). Plots of these regions can be found in Figure S11.

TFAM has high affinity for DNA and undergoes cooperative binding regardless of UVC-induced damage

The high-throughput binding assays reveal that TFAM exhibits DNA sequence preferences, but these preferences cannot be directly extrapolated to the binding affinity of TFAM to DNA, nor can they provide insight on the stoichiometry of binding. To investigate differences in TFAM binding affinity that may be associated with UVC-induced DNA damage, we performed fluorescence anisotropy and fit the binding curve to the Hill Equation [58] to determine the K_D and the extent of cooperative binding (n) (Methods). Sequences were selected to cover a range of z-scores identified in our array-based binding assays, and anisotropy experiments were performed on both undamaged and UVC-irradiated oligonucleotides. All sequences analyzed exhibit K_D values between 3 nM and 9 nM and n values between 1 and 5, indicating multiple TFAM proteins binding to each DNA. Overall, we do not observe any large differences in K_D or cooperativity values with or without UVC irradiation across any of the sequences analyzed (Figure S13, Table 2). This lack of correlation between the array-based binding data and the direct measurements of binding affinity contrasts with previous studies in which the occupancy of proteins at different DNA sequences, measured on high-density DNA arrays, directly correlates with the binding affinity [48,59], and suggests that the differences in TFAM occupancy may result from differences in extents of cooperative binding that is not discernable in the fluorescence anisotropy experiments.

To further examine the extent of oligomerization of TFAM on these DNA oligonucleotides and determine if there are any differences in TFAM binding on the "high" and "low" occupancy binders (selected according to the array-based binding occupancy measurements), we used atomic force microscopy (AFM) to examine the oligomeric state of TFAM in the absence and presence of one of the high and one of the low occupancy binders (Table 2). AFM is a powerful tool for determining the multimeric state of proteins, because the AFM volume correlates linearly with protein molecular weights [44,45] and AFM can be used to identify cooperative binding on small DNA oligonucleotides [47]. Inspection of the volume distributions of TFAM in the absence of DNA reveals a single peak at ~35 nm^3 with a tail to higher volumes, consistent with the dominant species being a monomer and a small amount of higher order species (Methods, Figure S14A). In the presence of the oligonucleotides, the volume distribution shifts to higher volumes that are consistent with dimers and higher order species (Figure S14B, C). Notably the "high binder" shows two distinct peaks at ~50nm^3 and 110 nm^3, consistent with cooperative assembly of a dimer and tetramer of TFAM on this oligonucleotide. In contrast, the "low binder" exhibits a broad distribution with a peak at ~50

nm^3 and a long tail to higher volumes, consistent with the cooperative formation of a dimer followed by weaker assembly of higher order species. This is consistent with previous SEC-MALS studies showing that TFAM oligomerization can differ with varying sequences [60]. These observations in differences in binding properties may not be captured in the fluorescence anisotropy measurement and therefore may account for the lack of correlation between the high-throughput array-based binding data and the binding affinities measured by fluorescence anisotropy.

Table 2: TFAM K_D measurements:

Sequence	-UV			+UV		
	Array z-score percentile	**K_D ± SEM (nM)**	**n ± SEM**	**Array z-score percentile**	**K_D ± SEM (nM)**	**n ± SEM**
ND4_473*	0.48	4.95 ± 0.03	5.06 ± 0.09	28.28	5.36 ± 0.14	4.76 ± 0.11
ND2_401	25.32	4.36 ± 0.24	2.64 ± 0.22	23.62	6.24 ± 0.15	2.61 ± 0.25
ND3_92	25.68	4.53 ± 0.13	2.63 ± 0.22	10.23	5.54 ± 0.14	2.19 ± 0.06
RNR2_619	25.71	4.89 ± 0.33	2.46 ± 0.23	51.19	8.13 ± 0.39	2.33 ± 0.10
COX1_27	75.32	6.09 ± 0.43	2.07 ± 0.07	74.45	5.90 ± 0.10	2.12 ± 0.28
ND1_288	75.16	3.41 ± 0.03	3.04 ± 0.19	35.79	6.12 ± 0.22	1.90 ± 0.12
ND6_87	75.74	5.20 ± 0.32	2.84 ± 0.14	95.50	7.63 ± 0.21	2.27 ± 0.26
ND1_450	90.25	4.33 ± 0.17	2.40 ± 0.43	70.40	6.36 ± 0.51	2.20 ± 0.13
COX2_229	90.78	3.94 ± 0.03	2.77 ± 0.17	80.81	4.87 ± 0.35	2.18 ± 0.14
TRNT_10	90.90	4.24 ± 0.12	2.15 ± 0.24	96.07	7.79 ± 0.80	1.81 ± 0.05
ND1_353 40mer	99.99	5.69 ± 0.15	3.09 ± 0.11	94.24	7.25 ± 0.39	4.38 ± 0.33
ND1_353**	99.99	7.56 ± 0.34	3.85 ± 0.49	94.24	7.66 ± 0.88	2.94 ± 0.40

* Represents a low occupancy sequence in the array-based TFAM binding data, referred to as "low binder"
** Represents a high occupancy sequence in the array-based TFAM binding data, referred to as "high binder"

TFAM compacts UVC-damaged DNA more efficiently than undamaged DNA:

The array-based TFAM binding data indicate that the relative occupancy of TFAM for sequences in the mitochondrial genome change upon irradiation, with lower specificity associated with irradiation. Because one of the roles of TFAM is to compact the mitochondrial genome into nucleoid structures [9,10], we examined the impact of UVC-induced DNA damage on nucleoid structure using AFM. For these experiments, we used circular plasmid DNA (pUC19) that was either untreated or exposed to 100 J/m^2 UVC, which introduces roughly three photolesions per plasmid (Methods). We incubated the damaged or undamaged DNA with

TFAM for two minutes before depositing the sample on the mica surface. We used low concentrations of TFAM (15 nM or 30 nM) to capture the differences, if any, in the extents of compaction and to prevent full compaction of the DNA.

Figure 4A shows images of pUC19 alone as well as undamaged and damaged pUC19 with 30 nM TFAM. The AFM images show that in the absence of TFAM, the plasmid is well spread on the surface. In contrast, TFAM promotes the formation of both punctate and disperse protein assemblies, as well as tracts of protein along the DNA, which often bridge two regions of DNA together (Figure 4A, S15, S16). Notably, most DNAs show only a single cluster of proteins, with the majority of the rest of the DNA being unbound. In fact, at 15 nM TFAM a significant percent of the DNAs have no protein bound, while other DNA molecules have punctate assemblies (Figure S16). These observations indicate that TFAM is cooperatively assembling on the DNA, consistent with previous work indicating TFAM is highly cooperative [61], both in the presence and absence of irradiation.

To assess the extent of compaction we measured the total volume of the DNA and its associated proteins on DNA (hereafter referred to as "complexes") (Methods). In the absence of protein, the distribution of volumes shows a single peak centered at ~5000 nm^3 (Figure 4B). Addition of 15 nM and 30 nM TFAM results in the distributions broadening and shifting to higher volumes with increasing TFAM concentration in both the absence and presence of UVC irradiation. Notably, the volumes for the irradiated DNAs are greater than those without irradiation: the volumes for samples with irradiated DNA at 15 nM and 30 nM TFAM are ~12,600 nm^3 and ~12,700 nm^3, respectively, and the samples without irradiation at 15 nM and 30nM TFAM are ~8,250 nm^3 and ~7,500 nm^3, respectively (Figure 4B). These results suggest that UVC irradiation increases the cooperative assembly of TFAM on pUC19. Inspection of the AFM images reveals that these differences in volume are associated with differences in compaction of the DNA. Specifically, addition of TFAM to UVC irradiated DNA results in more compact and punctate structures relative to undamaged DNA, which shows proteins that appear to be more loosely associated with the DNA (Figure 4A, 4C, S15).

To quantitatively assess the differences in compaction, we categorized each TFAM-pUC19 complex as: free DNA, dispersed (small clusters with no protein tracts on DNA), intermediate (small clusters with protein tracts), and punctate (tightly associated punctate clusters) (Figure 4C). At 15 nM TFAM, the majority of the DNAs (~55%) have no protein bound with very few punctate species with unirradiated DNA; whereas, the irradiated DNA shows significantly lower percentage of free DNA and an increase of punctate structures (Figure 4D). At 30 nM TFAM, most of the DNAs show dispersed (~35%) and intermediate (~60%) species on unirradiated DNA and intermediate (~30%) and punctate (~60%) species on irradiated DNA. Taken together, these results indicate that DNA damage promotes compaction of DNA by TFAM (Figure 4E).

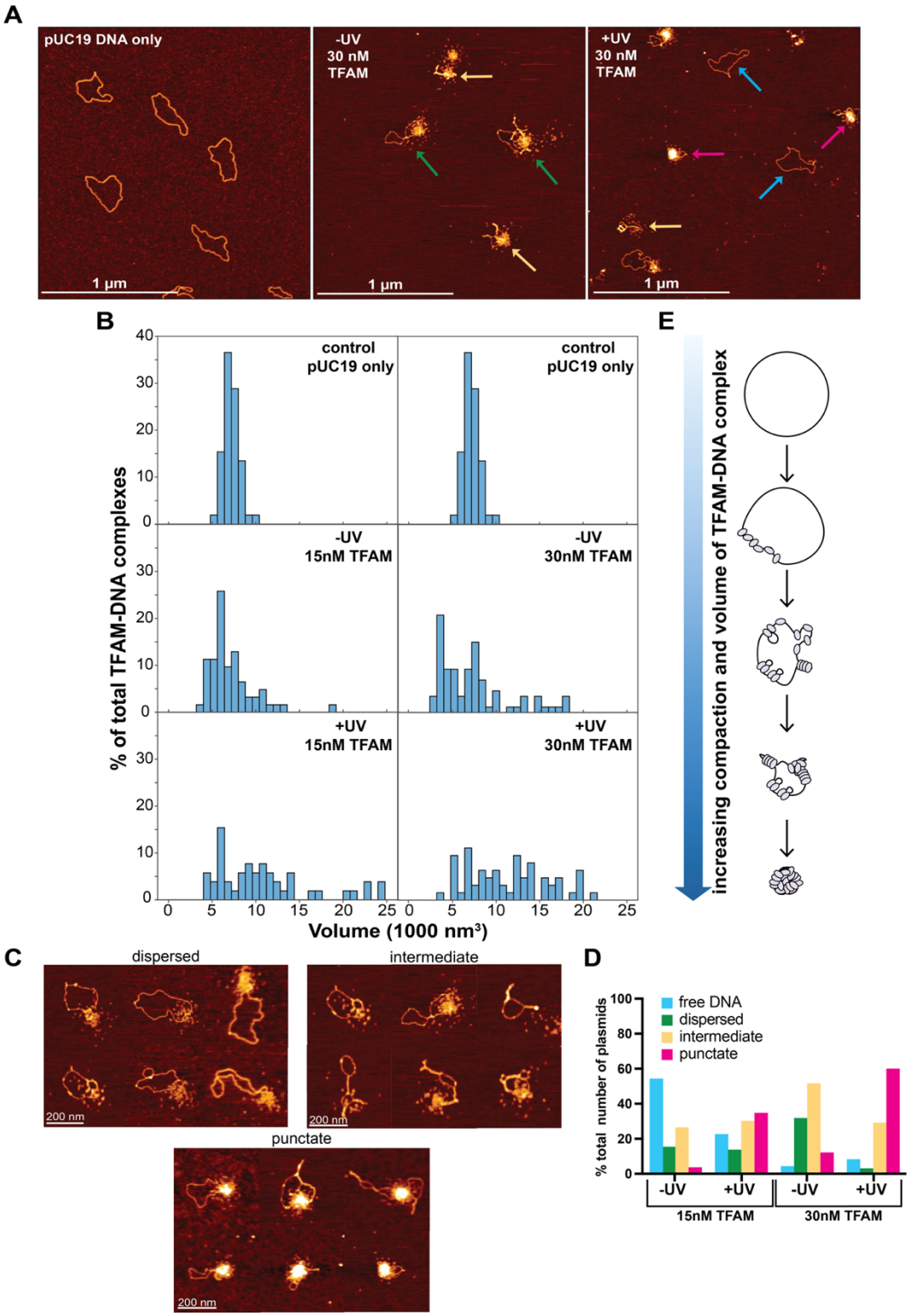

Figure 4: Atomic force microscopy of TFAM-DNA substrates indicates an increase in compaction associated with UVC exposure. A) AFM images of the pUC19 DNA only (control) and the 30 nM TFAM-DNA complexes in two different conditions: one with (+UV) or without (-UV) UVC irradiated DNA. Colored arrows on the AFM images represent the different

TFAM-DNA complexes categorizations: dispersed (green), intermediate (yellow), punctate (red), and free DNA (blue). The white scale bar represents 1 μm. **B)** Histogram plot of the volumes distribution of plasmid DNA only (control) as well as the 15 nM and 30 nM TFAM-DNA complexes with (+UV) or without (-UV) UVC damaged DNA. All axes in the histogram are scaled the same. The data for control pUC19 only was replicated for each TFAM concentration for clarity in comparisons. **C)** Atomic force microscopy images of three different TFAM-DNA complex categorizations labeled as dispersed (small clusters with no protein tracts on DNA), intermediate (small clusters with protein tracts), and punctate (tightly associated punctate clusters). The white scale bar represents 200 nm. **D)** A bar graph representing the percent total number of plasmids in the 15nM TFAM concentration with (+UV) or without (-UV) UVC damaged DNA and the 30nM TFAM concentration with (+UV) or without (-UV) UVC damaged DNA. **E)** Schematic of the TFAM-DNA binding and compaction mechanism.

Increased compaction of mtDNA nucleoids does not offer protection from UVC-induced mtDNA damage or alter damage removal rates:

Recent evidence shows that nucleoid compaction varies throughout cellular differentiation and between cell types [13]. It is well known that chromatin both protects from various forms of DNA damage and regulates DNA repair activities [62,63]; however, little is known about the role of DNA compaction in the mitochondria. Although it has been proposed that the mitochondrial nucleoid may protect mtDNA from damage [14], there is no direct evidence supporting this. Our observation that TFAM compacts damaged DNA suggests that mtDNA compaction may play a role in protecting the cell from damaged mtDNA. To examine these possibilities, we tested whether overexpressing TFAM, which has been shown to increase mtDNA compaction in cells [13], would protect mtDNA from DNA damage or promote the removal of damaged mtDNA.

Following a 48-hour pretreatment with doxycycline (schematic in Figure 5A), we observe a two-fold induction of TFAM at the protein level, measured by western blot (Figure 5B, quantified in Figure 5C), as well as an increase in mRNA levels (Figure 5D). Elevated TFAM levels are sustained throughout the duration of the experiment (Figure 5B, Figure 5C, Figure 5D). To test whether increased TFAM expression is associated with protection of mtDNA from UVC-induced DNA damage, we exposed these cells to UVC and quantified the amount of mtDNA damage they received. Across a range of UVC doses, there are no differences in the lesion frequency between the control and TFAM overexpressing cells (Figure 5E). Additionally, overexpression of TFAM and the associated increase in nucleoid compaction does not influence the rate at which mtDNA damage is removed, evidenced by the similar lesion frequencies observed 24 hours and 48 hours following the UVC exposure (Figure 5F, Figure 5G), nor does overexpression of TFAM protect the cells from a loss of cell viability following exposure to UVC (Figure S17).

To complement these findings and test if the level of compaction of the mitochondrial nucleoid is protective against mtDNA damage across a wider range of TFAM concentrations, we

generated *in vitro* reconstituted nucleoids with full-length human mtDNA and varying amounts of TFAM. We generated a series of dose-response curves for UVC to determine if elevated TFAM levels are associated with protection from UVC-induced DNA damage. The conformational status of the mtDNA nucleoids was confirmed using AFM (Figure 5H). Again, we observe that increased nucleoid compaction, driven by elevated TFAM concentrations, is not sufficient to protect mtDNA from UVC-induced lesions (Figure 5I). Taken together, these results indicate that the degree of TFAM mediated compaction of mtDNA does not protect the DNA from UVC-induced DNA damage or increase the rate of removal of mtDNA damage.

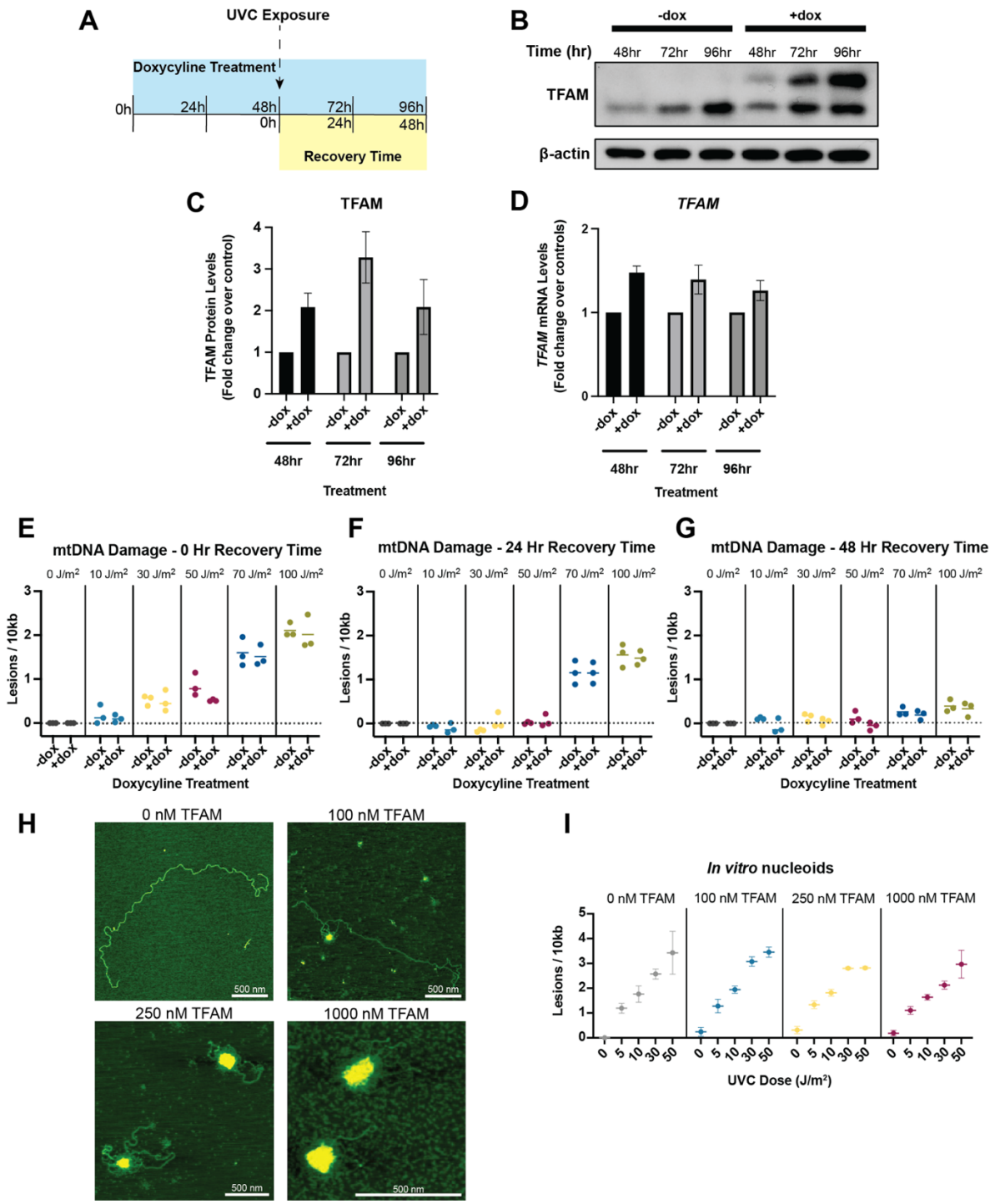

Figure 5: Increased nucleoid compaction does not protect mtDNA from UVC-induced DNA damage or alter damage removal rates.

A) Exposure paradigm for TFAM overexpression experiments. Cells were exposed to doxycycline for 48 hours prior to UVC exposure to ensure upregulation of TFAM at the time of exposure. Protein was quantified in control cells only to ensure TFAM upregulation. **B)** Representative western blot of TFAM-tetON cell lysates following 48, 72, and 96 hours of

doxycycline treatment to confirm TFAM upregulation. TFAM-tetON cells contain an HA tag that when expressed, results in a second band. **C)** Pixel quantifications of n=3 western blots shown in panel (B) at each time point. TFAM protein levels were normalized to β-actin and then normalized to the non-doxycycline treated controls. X-axis represents the doxycycline treatment and y-axis represents the fold change relative to the non-doxycycline treated cells. Data was analyzed via two-way ANOVA (doxycycline treatment p=0.0006, time p=0.25, interaction p=0.25). **D)** *TFAM* mRNA quantification following doxycycline treatment. X-axis represents the doxycycline treatment and y-axis represents the fold change relative to the non-doxycycline treated cells. Data was analyzed via two-way ANOVA (doxycycline treatment p=0.0003, time p=0.52, interaction p=0.52). **E)** Lesion frequency following UVC exposure in TFAM-tetON cells immediately after the exposure (0-hour recovery time). X-axis represents the doxycycline treatment across a range of UVC doses and y-axis represents the lesion frequency (lesions per 10kb). Data was analyzed via two-way ANOVA (UVC dose: p<0.0001, doxycycline treatment p=0.15, interaction: p=0.77). **F)** Lesion frequency following UVC exposure in TFAM-tetON cells 24 hours after the exposure (24-hour recovery time). X-axis represents the doxycycline treatment across a range of UVC doses and y-axis represents the lesion frequency (lesions per 10kb). Data was analyzed via two-way ANOVA (UVC dose: p<0.0001, doxycycline treatment p=0.71, interaction: p=0.65). **G)** Lesion frequency following UVC exposure in TFAM-tetON cells 48 hours after the exposure (48-hour recovery time). X-axis represents the doxycycline treatment across a range of UVC doses and y-axis represents the lesion frequency (lesions per 10kb). Data was analyzed via two-way ANOVA (UVC dose: p<0.0001, doxycycline treatment p=0.01, interaction: p=0.61). **H)** Representative AFM images of *in vitro* nucleoids generated using purified TFAM and PCR amplified human mtDNA at 0, 100, 250, and 1000 nM TFAM. All scale bars represent 500 nm. **I)** Lesion frequency following UVC exposure in *in vitro* nucleoids. X-axis represents the UVC dose and y-axis represents the lesion frequency (lesions per 10kb). Data was analyzed via two-way ANOVA (UVC dose: p<0.0001, TFAM concentration p=0.20, interaction: p=0.86).

Discussion:

The mechanisms by which cells handle mtDNA damage remain poorly understood. In particular, the absence of NER in mitochondria begs the question of how bulky lesions in mtDNA are removed. TFAM is a multifunctional protein that regulates both transcription and replication of mtDNA, and it compacts the genome into nucleoids. Previous studies suggest that TFAM may protect the DNA from damage [14] and serve as a damage sensing protein [26]. In this work, we investigate cellular responses to low levels of mtDNA damage caused by UVC irradiation as well as the effect of UVC damage on TFAM-DNA interactions. These studies suggest that although TFAM does not protect against UVC-induced DNA damage, it may function as a photolesion DNA damage sensor.

Mitochondria respond to UVC-induced mtDNA damage in the absence of apparent mitochondrial dysfunction:

Exposure to UVC that induces mtDNA damage results in a host of responses, including removal of damaged mtDNA and an increase in mtDNA replication to replenish mtDNA copy number (Figure 1, 2). The removal of damaged mtDNA begins within the first 24 hours after damage exposure (Figure 1 and 2). This removal is followed by upregulation of *TFAM*, *POLG*, and *POLRMT*, which initiate and carry out mtDNA replication, allowing replenishment of mtDNA (Figure 2). Once mtDNA levels have recovered (48 hours), cells upregulate *TFAM* and *POLRMT* as well as transcriptional activity on mtDNA (measured by upregulation of *ND-1*) (Figure 2), likely to replenish mtRNA and protein levels. These damage-induced changes to mtDNA transcription and replication, including transcription of nuclear-encoded genes (*TFAM*, *POLG*, *POLRMT*), occurred in the absence of apparent mitochondrial dysfunction, suggesting the possibility that cells might directly detect such damage.

TFAM exhibits preferential binding to a large number of sequences in the mitochondrial genome:

Examination of the array-based binding data reveal that in the absence of damage, TFAM shows a wide range of z-scores across the mitochondrial genomic sequences (Figure 3), indicating preference of certain sequences. Notably, the sequences with high z-scores are not associated with the proposed $GN_{10}G$ motif, which was previously suggested as a consensus sequence for TFAM (Figure S9) [32]. In addition, we found that the z-scores at promoter sites were modest compared to other regions in the genome (Figure 3 and Figure S11), which is consistent with previous work characterizing TFAM binding across the mitochondrial genome via ChIP-seq [55]. These findings indicate that unlike most transcription factors, TFAM by itself shows low specificity for its promoters, with the exception of LSP1, and suggest that TFAM may require interactions with additional proteins present in the nucleoid to promote transcription. Indeed, recent work from Tan *et al*. (Figure S4a) [57] indicates that POLRMT and TFB2M are also needed, in addition to TFAM, to produce a notable enrichment of TFAM at the HSP1 and LSP2 promoters. Although we do not see strong binding signal at the promoter sites other than LSP1, the preferential binding of TFAM to sequences across the genome may be involved with facilitating compaction of the genome, which could in turn regulate transcription and replication. Specifically, the extent of the compaction of the mitochondrial genome is inversely proportional to the transcription and replication activity [14], similar to nucleosomes.

TFAM does not protect from UVC irradiation but may serve as a DNA damage sensor:

Previous studies have indicated that TFAM promotes DNA compaction [9,10]. Examination of complexes of TFAM bound to pUC19 and linear full length human mtDNA using AFM show that TFAM promotes compaction of both DNAs, with the extent of compaction dependent on TFAM concentration (Figure 4A, S16, 5H). At low TFAM concentrations, we observe small

punctate complexes with tracts along the DNA (Figure S16) which convert into large punctate complexes at higher TFAM concentrations (Figure 4A).

In the nuclear genome, compaction of DNA serves to protect DNA from damage as well as regulate expression, replication, and repair of DNA. Mitochondrial nucleoid compaction is believed to be associated with regulatory properties such as expression and replication [14]. TFAM-induced DNA compaction has been shown to protect mtDNA from enzymatic processes used in techniques such as Fiber-seq [13]; however, it remains unknown if TFAM protects DNA from damage. To determine if nucleoid compaction protects DNA from UVC-induced damage, we utilized both *in vitro* reconstituted nucleoids and an inducible TFAM overexpression cell model to investigate whether the compactional state of mitochondrial nucleoids serves to protect the DNA from damage. *In vitro*, even at the highest concentration of TFAM, where the entire mtDNA appears compact in AFM images, we observe no protection of DNA from UVC (Figure 5H, Figure 5I). Similarly, in cells where TFAM is overexpressed, which should produce increased compaction of nucleoids [13], we observe no protection from UVC-induced DNA damage or changes in removal rates of the damage (Figure 5E, F, G). Taken together, these results indicate that TFAM does not protect DNA from UVC-induced DNA damage. Notably, however, our AFM and array-based binding data suggest that TFAM may act as a damage sensor.

Our AFM data show significantly increased TFAM-mediated compaction of irradiated vs unirradiated pUC19 DNA (Figure 4). Specifically, in the presence of irradiation, TFAM promotes compact nucleoid structures, whereas in the absence of irradiation, the TFAM clusters are more loosely associated (Figure 4, S16). These results suggest that UVC irradiation promotes the cooperative assembly of TFAM on DNA. These TFAM assemblies do not appear to supercoil the DNA, but rather appear to bring distal DNA segments together, consistent with previous studies (Figure 4, S16) [9]. As such, UVC lesions could potentially serve as nucleation sites for TFAM assemblies, and these local clusters may come together to form a compact nucleoid structure containing large regions of the DNA. This suggestion is consistent with laser tweezer studies on stretched DNA that showed formation of multiple small linear clusters of TFAM that can come together to form a larger linear cluster [61]. In our studies, the DNA is not stretched and therefore, the TFAM assemblies can come together through space to form compact nucleoids formed via TFAM-DNA interactions that promote further oligomerization of TFAM with itself. Notably, UVC appears to significantly stabilize TFAM-TFAM interactions to promote a compact nucleoid.

Our high-throughput TFAM binding data reveal a redistribution of z-scores upon UVC irradiation, with more uniform distributions of TFAM occupancy across the genomic sequences for the irradiated than unirradiated DNAs (Figure 3). The observed reduction in sequence specificity in the context of UVC irradiation suggests that TFAM occupation at UVC-irradiated DNA outcompetes any sequence specificity it has. These data would represent an extensively damaged genome because the DNA was irradiated at a high dose of UVC, 1500 J/m^2. In contrast, the DNA in the AFM experiments contain on average approximately three lesions per plasmid.

Strikingly, the significant increase in compaction as evidenced by the increase in punctate structures of pUC19 by TFAM in the presence of UVC irradiation (Figure 4D) suggests that only a few lesions are sufficient to drive dramatic compaction of pUC19.

In our AFM images, we observe tracts of protein binding along the DNA that bridge two regions of DNA together (Figure 4A, 4C, S15, S16) in a zipper-like manner, without inducing any significant supercoiling. These results are consistent with previous studies [9,10]. In contrast, the X-ray crystal structures of TFAM bound to DNA show the protein wrapped around the DNA, forming a U-turn bend in the DNA [28,30,31]. This mode of binding to plasmid DNA would induce supercoiling [64]. Taken together, these results indicate that TFAM can bind DNA in at least two different states; one which induces a U-turn bend in the DNA and one that does not dramatically distort the DNA. In the AFM images, in general, we observe a single cluster of TFAM per plasmid, with or without adjacent fiber formation. In the absence of UV irradiation, the clusters occupy a smaller region of DNA and exist in looser, more intermediate states (Figure 4D), whereas in the irradiated DNA, TFAM forms more punctate clusters that contain more of the plasmid DNA (Figure 4D). One possible explanation for how only a few lesions could promote increased compaction of the DNA by TFAM is that TFAM may preferentially bind UV damage, which distorts DNA, in the U-turn mode. This U-turn in the DNA would bring two DNA double strands close to one another and therefore promote local zipping up of the DNA. Subsequently, these clusters may cooperatively assemble together to form tight compact structures (Figure 4C, 4E).

Conclusions:

Overall, we found that cellular responses to mtDNA damage including increased mtDNA turnover, upregulation of mtDNA replication machinery, and increased mtRNA transcription occur in the absence of loss of mitochondrial membrane potential. We identified TFAM as a potential DNA damage sensor in that it promotes UVC-dependent conformational changes in the nucleoids, making them more compact. The increased compaction may serve to signal damage in the mitochondrial genome. For example, once "tagged" by TFAM, damaged mtDNAs might be actively removed via mitophagy [21,25], autophagy [20], extracellular export, TFAM-mediated nucleoid-phagy [65], or by more recently-identified non-autophagic pathways [66,67] (Figure 6). Alternately, simply by removing these damaged genomes from the pool that is actively used for transcription and replication, TFAM-mediated compaction could serve to store damaged genomes until they are removed passively by normal mtDNA turnover processes (Figure 6). In any case, these non-repair pathways for removing mtDNA damage may provide a mechanism for preventing mtDNA mutagenesis. Additional work will be required to test these possibilities *in vivo*.

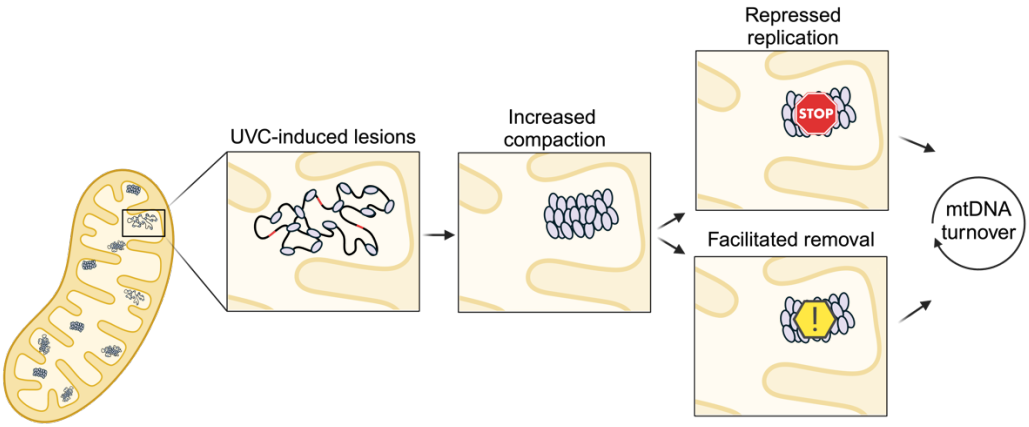

Figure 6: Proposed cellular model of the role of TFAM in mtDNA damage sensing. Alterations in TFAM-DNA interactions may alter compactional status of mitochondrial nucleoids. This feature may serve to "tag" mitochondrial genomes as damaged, which could lend itself to repression of the replication of damaged genomes, flagging damaged genomes for targeted degradation, or both. Both active removal and repression of replication would allow for removal of damaged genomes during mtDNA turnover processes and provide a mechanism for preventing mtDNA mutagenesis. Figure made in BioRender.

Acknowledgements:
We thank the UNC Macromolecular Interactions Facility for providing instrumentation for fluorescence anisotropy as well as the Duke Light Microscopy Core for providing access to microscopes and image analysis software.

Funding: This work was supported by the National Science Foundation award GRFP DGE-1644868 to DEK, NIEHS P42ES010356 to JNM, NIEHS T32ES021432 to JNM, NIGMS R35 GM127151 to DE, NSF/MCB 2324614 to RG, and P30CA016086 to the UNC Center for Structural Biology.

Author Contributions:
DEK: conceptualization, investigation, formal analysis, writing – original draft
EEB: investigation, formal analysis, writing – original draft
MJS: investigation, formal analysis, visualization, writing – original draft

IR: investigation, formal analysis
AG: investigation, formal analysis
CJ: investigation, formal analysis
ELD: investigation, formal analysis
YZ: investigation, formal analysis
WZ: investigation, formal analysis
HW: investigation, formal analysis
EC: investigation, formal analysis
SKM: funding acquisition, supervision
DE: conceptualization, funding acquisition, supervision, writing – original draft
RG: conceptualization, funding acquisition, supervision, writing – original draft
JNM: conceptualization, funding acquisition, supervision, writing – original draft

Declaration of Interests:
The authors have no interests to declare.

References:

1. Picard, M., and Shirihai, O.S. (2022). Mitochondrial signal transduction. Cell Metabolism *34*, 1620-1653. https://doi.org/10.1016/j.cmet.2022.10.008.
2. Gustafsson, C.M., Falkenberg, M., and Larsson, N.G. (2016). Maintenance and Expression of Mammalian Mitochondrial DNA. Annu Rev Biochem *85*, 133-160. 10.1146/annurev-biochem-060815-014402.
3. Lee, S.R., and Han, J. (2017). Mitochondrial Nucleoid: Shield and Switch of the Mitochondrial Genome. Oxid Med Cell Longev *2017*, 8060949-8060949. 10.1155/2017/8060949.
4. Iborra, F.J., Kimura, H., and Cook, P.R. (2004). The functional organization of mitochondrial genomes in human cells. BMC Biol *2*, 9. 10.1186/1741-7007-2-9.
5. Bogenhagen, D.F. (2012). Mitochondrial DNA nucleoid structure. Biochimica et Biophysica Acta (BBA) - Gene Regulatory Mechanisms *1819*, 914-920. https://doi.org/10.1016/j.bbagrm.2011.11.005.
6. Spelbrink, J.N. (2010). Functional organization of mammalian mitochondrial DNA in nucleoids: history, recent developments, and future challenges. IUBMB Life *62*, 19-32. 10.1002/iub.282.
7. Bogenhagen, D.F., Wang, Y., Shen, E.L., and Kobayashi, R. (2003). Protein components of mitochondrial DNA nucleoids in higher eukaryotes. Mol Cell Proteomics *2*, 1205-1216. 10.1074/mcp.M300035-MCP200.
8. Rebelo, A.P., Dillon, L.M., and Moraes, C.T. (2011). Mitochondrial DNA transcription regulation and nucleoid organization. J Inherit Metab Dis *34*, 941-951. 10.1007/s10545-011-9330-8.
9. Kukat, C., Davies, K.M., Wurm, C.A., Spåhr, H., Bonekamp, N.A., Kühl, I., Joos, F., Polosa, P.L., Park, C.B., Posse, V., et al. (2015). Cross-strand binding of TFAM to a single mtDNA molecule forms the mitochondrial nucleoid. Proceedings of the National Academy of Sciences *112*, 11288-11293. 10.1073/pnas.1512131112.
10. Kaufman, B.A., Durisic, N., Mativetsky, J.M., Costantino, S., Hancock, M.A., Grutter, P., and Shoubridge, E.A. (2007). The Mitochondrial Transcription Factor TFAM Coordinates

the Assembly of Multiple DNA Molecules into Nucleoid-like Structures. Molecular Biology of the Cell *18*, 3225-3236. 10.1091/mbc.e07-05-0404.
11. Wachsmuth, M., Hübner, A., Li, M., Madea, B., and Stoneking, M. (2016). Age-Related and Heteroplasmy-Related Variation in Human mtDNA Copy Number. PLoS Genet *12*, e1005939. 10.1371/journal.pgen.1005939.
12. Schon, E.A. (2000). Mitochondrial genetics and disease. Trends Biochem Sci *25*, 555-560. 10.1016/s0968-0004(00)01688-1.
13. Isaac, R.S., Tullius, T.W., Hansen, K.G., Dubocanin, D., Couvillion, M., Stergachis, A.B., and Churchman, L.S. (2024). Single-nucleoid architecture reveals heterogeneous packaging of mitochondrial DNA. Nature Structural & Molecular Biology. 10.1038/s41594-024-01225-6.
14. Brüser, C., Keller-Findeisen, J., and Jakobs, S. (2021). The TFAM-to-mtDNA ratio defines inner-cellular nucleoid populations with distinct activity levels. Cell Reports *37*, 110000. https://doi.org/10.1016/j.celrep.2021.110000.
15. Zhao, L., and Sumberaz, P. (2020). Mitochondrial DNA Damage: Prevalence, Biological Consequence, and Emerging Pathways. Chem Res Toxicol *33*, 2491-2502. 10.1021/acs.chemrestox.0c00083.
16. Meyer, J.N., Leung, M.C., Rooney, J.P., Sendoel, A., Hengartner, M.O., Kisby, G.E., and Bess, A.S. (2013). Mitochondria as a target of environmental toxicants. Toxicol Sci *134*, 1-17. 10.1093/toxsci/kft102.
17. Alexeyev, M., Shokolenko, I., Wilson, G., and LeDoux, S. (2013). The maintenance of mitochondrial DNA integrity--critical analysis and update. Cold Spring Harb Perspect Biol *5*, a012641. 10.1101/cshperspect.a012641.
18. Gustafson, M.A., Sullivan, E.D., and Copeland, W.C. (2020). Consequences of compromised mitochondrial genome integrity. DNA Repair (Amst) *93*, 102916. 10.1016/j.dnarep.2020.102916.
19. Gillet, L.C., and Scharer, O.D. (2006). Molecular mechanisms of mammalian global genome nucleotide excision repair. Chem Rev *106*, 253-276. 10.1021/cr040483f.
20. Bess, A.S., Ryde, I.T., Hinton, D.E., and Meyer, J.N. (2013). UVC-induced mitochondrial degradation via autophagy correlates with mtDNA damage removal in primary human fibroblasts. J Biochem Mol Toxicol *27*, 28-41. 10.1002/jbt.21440.
21. Bess, A.S., Crocker, T.L., Ryde, I.T., and Meyer, J.N. (2012). Mitochondrial dynamics and autophagy aid in removal of persistent mitochondrial DNA damage in Caenorhabditis elegans. Nucleic Acids Res *40*, 7916-7931. 10.1093/nar/gks532.
22. Valenci, I., Yonai, L., Bar-Yaacov, D., Mishmar, D., and Ben-Zvi, A. (2015). Parkin modulates heteroplasmy of truncated mtDNA in Caenorhabditis elegans. Mitochondrion *20*, 64-70. 10.1016/j.mito.2014.11.001.
23. Pickrell, A.M., Huang, C.H., Kennedy, S.R., Ordureau, A., Sideris, D.P., Hoekstra, J.G., Harper, J.W., and Youle, R.J. (2015). Endogenous Parkin Preserves Dopaminergic Substantia Nigral Neurons following Mitochondrial DNA Mutagenic Stress. Neuron *87*, 371-381. 10.1016/j.neuron.2015.06.034.
24. Valente, W.J., Ericson, N.G., Long, A.S., White, P.A., Marchetti, F., and Bielas, J.H. (2016). Mitochondrial DNA exhibits resistance to induced point and deletion mutations. Nucleic Acids Res *44*, 8513-8524. 10.1093/nar/gkw716.
25. Leuthner, T.C., Benzing, L., Kohrn, B.F., Bergemann, C.M., Hipp, M.J., Hershberger, K.A., Mello, D.F., Sokolskyi, T., Stevenson, K., Merutka, I.R., et al. (2022). Resistance of mitochondrial DNA to cadmium and Aflatoxin B1 damage-induced germline mutation accumulation in C. elegans. Nucleic Acids Res *50*, 8626-8642. 10.1093/nar/gkac666.
26. Chew, K., and Zhao, L. (2021). Interactions of Mitochondrial Transcription Factor A with DNA Damage: Mechanistic Insights and Functional Implications. Genes (Basel) *12*. 10.3390/genes12081246.

27. Campbell, C.T., Kolesar, J.E., and Kaufman, B.A. (2012). Mitochondrial transcription factor A regulates mitochondrial transcription initiation, DNA packaging, and genome copy number. Biochim Biophys Acta *1819*, 921-929. 10.1016/j.bbagrm.2012.03.002.
28. Ngo, H.B., Lovely, G.A., Phillips, R., and Chan, D.C. (2014). Distinct structural features of TFAM drive mitochondrial DNA packaging versus transcriptional activation. Nat Commun *5*, 3077. 10.1038/ncomms4077.
29. Kang, D., Kim, S.H., and Hamasaki, N. (2007). Mitochondrial transcription factor A (TFAM): roles in maintenance of mtDNA and cellular functions. Mitochondrion *7*, 39-44. 10.1016/j.mito.2006.11.017.
30. Ngo, H.B., Kaiser, J.T., and Chan, D.C. (2011). The mitochondrial transcription and packaging factor Tfam imposes a U-turn on mitochondrial DNA. Nature Structural & Molecular Biology *18*, 1290-1296. 10.1038/nsmb.2159.
31. Rubio-Cosials, A., Sydow, J.F., Jiménez-Menéndez, N., Fernández-Millán, P., Montoya, J., Jacobs, H.T., Coll, M., Bernadó, P., and Solà, M. (2011). Human mitochondrial transcription factor A induces a U-turn structure in the light strand promoter. Nature Structural & Molecular Biology *18*, 1281-1289. 10.1038/nsmb.2160.
32. Choi, W.S., and Garcia-Diaz, M. (2022). A minimal motif for sequence recognition by mitochondrial transcription factor A (TFAM). Nucleic Acids Res *50*, 322-332. 10.1093/nar/gkab1230.
33. Yoshida, Y., Izumi, H., Ise, T., Uramoto, H., Torigoe, T., Ishiguchi, H., Murakami, T., Tanabe, M., Nakayama, Y., Itoh, H., et al. (2002). Human mitochondrial transcription factor A binds preferentially to oxidatively damaged DNA. Biochem Biophys Res Commun *295*, 945-951. 10.1016/s0006-291x(02)00757-x.
34. Canugovi, C., Maynard, S., Bayne, A.C., Sykora, P., Tian, J., de Souza-Pinto, N.C., Croteau, D.L., and Bohr, V.A. (2010). The mitochondrial transcription factor A functions in mitochondrial base excision repair. DNA Repair (Amst) *9*, 1080-1089. 10.1016/j.dnarep.2010.07.009.
35. Xu, W., Tang, J., and Zhao, L. (2023). DNA-protein cross-links between abasic DNA damage and mitochondrial transcription factor A (TFAM). Nucleic Acids Res *51*, 41-53. 10.1093/nar/gkac1214.
36. Yoshida, Y., Izumi, H., Torigoe, T., Ishiguchi, H., Itoh, H., Kang, D., and Kohno, K. (2003). p53 Physically Interacts with Mitochondrial Transcription Factor A and Differentially Regulates Binding to Damaged DNA1. Cancer Research *63*, 3729-3734.
37. Wong, T.S., Rajagopalan, S., Freund, S.M., Rutherford, T.J., Andreeva, A., Townsley, F.M., Petrovich, M., and Fersht, A.R. (2009). Biophysical characterizations of human mitochondrial transcription factor A and its binding to tumor suppressor p53. Nucleic Acids Res *37*, 6765-6783. 10.1093/nar/gkp750.
38. He, X., Wang, P., and Wang, Y. (2021). Mitochondrial Transcription Factor A Binds to and Promotes Mutagenic Transcriptional Bypass of O(4)-Alkylthymidine Lesions. Anal Chem *93*, 1161-1169. 10.1021/acs.analchem.0c04224.
39. Xu, W., Boyd, R.M., Tree, M.O., Samkari, F., and Zhao, L. (2019). Mitochondrial transcription factor A promotes DNA strand cleavage at abasic sites. Proc Natl Acad Sci U S A *116*, 17792-17799. 10.1073/pnas.1911252116.
40. Arzt, M., Deschamps, J., Schmied, C., Pietzsch, T., Schmidt, D., Tomancak, P., Haase, R., and Jug, F. (2022). LABKIT: Labeling and Segmentation Toolkit for Big Image Data. Frontiers in Computer Science *4*. 10.3389/fcomp.2022.777728.
41. Lachmanovich, E., Shvartsman, D.E., Malka, Y., Botvin, C., Henis, Y.I., and Weiss, A.M. (2003). Co-localization analysis of complex formation among membrane proteins by computerized fluorescence microscopy: application to immunofluorescence co-patching studies. J Microsc *212*, 122-131. 10.1046/j.1365-2818.2003.01239.x.

42. Furda, A., Santos, J.H., Meyer, J.N., and Van Houten, B. (2014). Quantitative PCR-based measurement of nuclear and mitochondrial DNA damage and repair in mammalian cells. Methods Mol Biol *1105*, 419-437. 10.1007/978-1-62703-739-6_31.
43. Colton, M.D., Kwok, K.W., Brandon, J.A., Warren, I.H., Ryde, I.T., Cooper, E.M., Hinton, D.E., Rittschof, D., and Meyer, J.N. (2014). Developmental toxicity and DNA damage from exposure to parking lot runoff retention pond samples in the Japanese medaka (Oryzias latipes). Mar Environ Res *99*, 117-124. 10.1016/j.marenvres.2014.04.007.
44. Ratcliff, G.C., and Erie, D.A. (2001). A Novel Single-Molecule Study To Determine Protein−Protein Association Constants. Journal of the American Chemical Society *123*, 5632-5635. 10.1021/ja005750n.
45. Yang, Y., Wang, H., and Erie, D.A. (2003). Quantitative characterization of biomolecular assemblies and interactions using atomic force microscopy. Methods *29*, 175-187. 10.1016/s1046-2023(02)00308-0.
46. Brar, S.S., Sacho, E.J., Tessmer, I., Croteau, D.L., Erie, D.A., and Diaz, M. (2008). Activation-induced deaminase, AID, is catalytically active as a monomer on single-stranded DNA. DNA Repair (Amst) *7*, 77-87. 10.1016/j.dnarep.2007.08.002.
47. Chelico, L., Sacho, E.J., Erie, D.A., and Goodman, M.F. (2008). A model for oligomeric regulation of APOBEC3G cytosine deaminase-dependent restriction of HIV. J Biol Chem *283*, 13780-13791. 10.1074/jbc.M801004200.
48. Berger, M.F., Philippakis, A.A., Qureshi, A.M., He, F.S., Estep, P.W., 3rd, and Bulyk, M.L. (2006). Compact, universal DNA microarrays to comprehensively determine transcription-factor binding site specificities. Nat Biotechnol *24*, 1429-1435. 10.1038/nbt1246.
49. Mielko, Z., Zhang, Y., Sahay, H., Liu, Y., Schaich, M.A., Schnable, B., Morrison, A.M., Burdinski, D., Adar, S., Pufall, M., et al. (2023). UV irradiation remodels the specificity landscape of transcription factors. Proc Natl Acad Sci U S A *120*, e2217422120. 10.1073/pnas.2217422120.
50. Berger, M.F., and Bulyk, M.L. (2009). Universal protein-binding microarrays for the comprehensive characterization of the DNA-binding specificities of transcription factors. Nat Protoc *4*, 393-411. 10.1038/nprot.2008.195.
51. James, K. (2020). Data analysis toolkits. EnviDat.
52. Ekstrand, M.I., Falkenberg, M., Rantanen, A., Park, C.B., Gaspari, M., Hultenby, K., Rustin, P., Gustafsson, C.M., and Larsson, N.G. (2004). Mitochondrial transcription factor A regulates mtDNA copy number in mammals. Hum Mol Genet *13*, 935-944. 10.1093/hmg/ddh109.
53. Blumberg, A., Danko, C.G., Kundaje, A., and Mishmar, D. (2018). A common pattern of DNase I footprinting throughout the human mtDNA unveils clues for a chromatin-like organization. Genome Res *28*, 1158-1168. 10.1101/gr.230409.117.
54. Malarkey, C.S., Bestwick, M., Kuhlwilm, J.E., Shadel, G.S., and Churchill, M.E. (2012). Transcriptional activation by mitochondrial transcription factor A involves preferential distortion of promoter DNA. Nucleic Acids Res *40*, 614-624. 10.1093/nar/gkr787.
55. Wang, Y.E., Marinov, G.K., Wold, B.J., and Chan, D.C. (2013). Genome-wide analysis reveals coating of the mitochondrial genome by TFAM. PLoS One *8*, e74513. 10.1371/journal.pone.0074513.
56. Miralles Fusté, J., Shi, Y., Wanrooij, S., Zhu, X., Jemt, E., Persson, Ö., Sabouri, N., Gustafsson, C.M., and Falkenberg, M. (2014). In vivo occupancy of mitochondrial single-stranded DNA binding protein supports the strand displacement mode of DNA replication. PLoS Genet *10*, e1004832. 10.1371/journal.pgen.1004832.
57. Tan, B.G., Mutti, C.D., Shi, Y., Xie, X., Zhu, X., Silva-Pinheiro, P., Menger, K.E., Díaz-Maldonado, H., Wei, W., Nicholls, T.J., et al. (2022). The human mitochondrial genome

contains a second light strand promoter. Molecular Cell *82*, 3646-3660.e3649. 10.1016/j.molcel.2022.08.011.
58. Hill, A.V., Hill, A.V., and Paganini-Hill, A. (1910). The possible effects of the aggregation of the molecules of haemoglobin on its dissociation curves. The Journal of Physiology *40*, 4-7.
59. Afek, A., Shi, H., Rangadurai, A., Sahay, H., Senitzki, A., Xhani, S., Fang, M., Salinas, R., Mielko, Z., Pufall, M.A., et al. (2020). DNA mismatches reveal conformational penalties in protein-DNA recognition. Nature *587*, 291-296. 10.1038/s41586-020-2843-2.
60. Cuppari, A., Fernández-Millán, P., Battistini, F., Tarrés-Solé, A., Lyonnais, S., Iruela, G., Ruiz-López, E., Enciso, Y., Rubio-Cosials, A., Prohens, R., et al. (2019). DNA specificities modulate the binding of human transcription factor A to mitochondrial DNA control region. Nucleic Acids Res *47*, 6519-6537. 10.1093/nar/gkz406.
61. Farge, G., Laurens, N., Broekmans, O.D., van den Wildenberg, S.M., Dekker, L.C., Gaspari, M., Gustafsson, C.M., Peterman, E.J., Falkenberg, M., and Wuite, G.J. (2012). Protein sliding and DNA denaturation are essential for DNA organization by human mitochondrial transcription factor A. Nat Commun *3*, 1013. 10.1038/ncomms2001.
62. Takata, H., Hanafusa, T., Mori, T., Shimura, M., Iida, Y., Ishikawa, K., Yoshikawa, K., Yoshikawa, Y., and Maeshima, K. (2013). Chromatin compaction protects genomic DNA from radiation damage. PLoS One *8*, e75622. 10.1371/journal.pone.0075622.
63. Stadler, J., and Richly, H. (2017). Regulation of DNA Repair Mechanisms: How the Chromatin Environment Regulates the DNA Damage Response. Int J Mol Sci *18*. 10.3390/ijms18081715.
64. van Noort, J., Verbrugge, S., Goosen, N., Dekker, C., and Dame, R.T. (2004). Dual architectural roles of HU: formation of flexible hinges and rigid filaments. Proc Natl Acad Sci U S A *101*, 6969-6974. 10.1073/pnas.0308230101.
65. Liu, H., Zhen, C., Xie, J., Luo, Z., Zeng, L., Zhao, G., Lu, S., Zhuang, H., Fan, H., Li, X., et al. (2024). TFAM is an autophagy receptor that limits inflammation by binding to cytoplasmic mitochondrial DNA. Nature Cell Biology *26*, 878-891. 10.1038/s41556-024-01419-6.
66. Sen, A., Kallabis, S., Gaedke, F., Jüngst, C., Boix, J., Nüchel, J., Maliphol, K., Hofmann, J., Schauss, A.C., Krüger, M., et al. (2022). Mitochondrial membrane proteins and VPS35 orchestrate selective removal of mtDNA. Nat Commun *13*, 6704. 10.1038/s41467-022-34205-9.
67. Newman, L.E., Weiser Novak, S., Rojas, G.R., Tadepalle, N., Schiavon, C.R., Grotjahn, D.A., Towers, C.G., Tremblay, M., Donnelly, M.P., Ghosh, S., et al. (2024). Mitochondrial DNA replication stress triggers a pro-inflammatory endosomal pathway of nucleoid disposal. Nat Cell Biol *26*, 194-206. 10.1038/s41556-023-01343-1.